Achieving Freestanding Rich-Mixed-Valence $Mn_xCo_yS_z$/CNT Film Electrodes Toward Foldable Ultrahigh Volume Energy Density All-Solid-State Supercapacitors

Group Members

Yuewei Zhou, Hanyue Wang, Shiwen Fang

Instructor

Dr. Liangliang Xu

School

Nanjing Foreign Language School

Location

Nanjing, Jiangsu, P. R. China

November 30, 2018

Abstract

Energy storage devices with both outstanding foldability, reliability and high volumetric energy densities are required to meet flexible display, portable and wearable electronics. In this work, novel foldable freestanding thin electrodes of rich-mixed-valence $Mn_xCo_yS_z$/carbon nanotube are rationally designed and prepared through acid solution activation of a dense carbon nanotube film (CNTF) into hydrogel-like conductive matrix, growth of $Mn_xCo_y(CO_3)_{0.5}OH$ precursor on each CNT, followed by sulfidation via anion-exchange. The activation allows the CNTFs to be effectively expanded and also endows CNT surface with active groups, which transforms hydrophobic CNTFs to be highly hydrophilic for uniform growth of precursor, and control over concentration dependent sulfidation kinetics leads to a porous coating. New insights into dependence of electrochemical performance enhancement on crystal structure and atomic ratio are proposed. Our theoretical calculation indicates that increasing the Co/S atomic ratio leads to enlargement of both inter-atom distance and hole diameter in $Mn_xCo_yS_z$ cell, which is further confirmed by the experimental results. The optimal $MnCo_9S_{10}$/CNTF electrode shows a specific capacitance reaching 450 F cm^{-3} at 10 mA cm^{-2}, much higher than previously reported values for CNT-based electrodes, and also exhibits remarkable cycling stability with only 1.6% capacity loss after 10,000 cycles at a high current density of 80 mA cm^{-2}. Also, the excellent performance is attributed to fast electron/ion transfer and increased availability of active sites/interfaces. An asymmetric all-solid-state supercapacitor applying the $MnCo_9S_{10}$/CNTF electrode delivers exceptionally high volumetric energy density of 67 mW h cm^{-3} (at 10 W cm^{-3}). Particularly, integrated devices with adjustable output voltage can be obtained by connecting several supercapacitors in series, and there are no structural failure and capacity loss during repeated folding and hammering. This work opens a new route to high-performance power sources for wearable electronics.

***Keywords*:** Carbon Nanotubes, Ternary Transition Metal Sulfides, Flexible Electrodes, Electrochemical Energy-Storage

Highlights:

(1) New insights into dependence of electrochemical performance enhancement on the crystal structure and atomic ratio are proposed. Theoretical calculation combined experimental results demonstrate that increasing the Co/S atomic ratio results in enlargement of both inter-atom distance and hole diameter in $Mn_xCo_yS_z$ cell.

(2) An effective acid activation strategy is rationally developed to regenerate a dense CNT film into a flexible, robust, and highly conductive matrix with greatly enhanced internal space and surface wettability, which facilitates efficient growth of redox species on each CNT assuring high loading percentages.

(3) The optimal $MnCo_9S_{10}$/CNTF electrode has a specific capacitance of 450 F cm^{-3} at 10 mA cm^{-2}, and also exhibits remarkable cycling stability with only 1.6% capacity loss after 10,000 cycles at a high current density of 80 mA cm^{-2}, much superior over previously reported values for similar CNT-based electrodes.

(4) An asymmetric all-solid-state supercapacitor applying the $MnCo_9S_{10}$/CNTF electrode delivers exceptionally high volumetric energy density of 67 mW h cm^{-3} (at 10 W cm^{-3}). Particularly, there are no structural failure and capacity loss during repeated folding and hammering of integrated devices with adjustable output voltage.

List of Abbreviations

Abbreviation	Full name
EDLC	Electric Double-Layer Capacitor
CV	Cyclic Voltammetry
GCD	Galvanostatic Charge-Discharge
FCCVD	Floating Catalyst Chemical Vapor Deposition
DFT	Density-Functional Theory
PANI	Polyaniline
PPy	Polypyrrole
PEDOT	Poly(3,4-ethylene-dioxythiophene)
CNTs	Carbon Nanotubes
CNTF	Carbon Nanotube Film
GO	Graphene Oxide
rGO	Reduced Graphene Oxide
PDMS	Polydimethylsiloxane
TAA	Thioacetamide
BET	Brunauer-Emmett-Teller
TGA	Thermogravimetric Analysis
SEM	Scanning Electron Microscopy
HRTEM	High Resolution Transmission Electron Microscopy
SAED	Selected Area Electron Diffraction
EDS	Energy Dispersive X-ray Spectroscopy
ICP	Inductively Coupled Plasma
XRD	X-ray Diffraction
XPS	X-ray Photoelectron Spectroscopy
EIS	Electrochemical Impedance Spectroscopy

Table of Contents

Table List

Figure Captions

1. Introduction

To meet the power requirements of wearable electronics, developing flexible, foldable, lightweight, and high-performance power sources is highly required. All-solid-state supercapacitors (SCs) are emerged as very promising energy storage device owing to their advantages such as high power density, fast recharge capability, and long cycle life[1-3]. For miniaturized SCs, specific volumetric energy density based on an entire device is a more important evaluation parameter than specific gravimetric and areal ones because the former reflects total amount of the stored energy[4]. Therefore, realization of ultrahigh volumetric capacitance and energy density while assuring reliability under large deformations is of great significance.

Rapid development of carbon based assemblies such as carbon fiber cloth,[5-6] graphene paper,[7] and carbon nanotube film (CNTF)[8] has created substantial opportunities for the development of flexible SCs. Among them, CNTF is ultrathin, lightweight, stretchable, and bendable, thus has many advantages for flexible film-shape electrodes.[9–11] One-dimensional CNT with a large length-to-diameter ratio as an isolated assembly unit possesses many inherent advantages such as good electrical conductivity, large surface area, low density, high flexibility and strength, but in a CNT-assembled film, high CNT-CNT contact-resistance and small surface area greatly reduce capacitances of CNTFs. Especially for carbon materials based electrodes, high capacitance can only be achieved in nanometer thick thin films due to their electrical double-layer capacitance that stems from charge separation at the electrode/electrolyte interface, but for practical applications, sub-micrometer thick electrodes with high specific volumetric capacitances are highly desirable.

In order to further increase the capacitive properties of CNTFs, especially to obtain high volumetric capacitance rather than specific mass capacitance, CNTFs as a conductive matrix are usually loaded with other pseudo-capacitive materials that store charges via reversible redox reactions. However, a CNT film has dense network structures with low internal space and hydrophobic surface, which tends to block the electrolyte wetting and ionic diffusion from the surface to the interior of the film, leading to a low loading merely at the film surface and thus the large inner space of the CNTFs cannot be utilized. While the synthesis of CNT-based composite films has made great progress, e.g., high performance film electrodes using CNTFs coated with conducting polymers (such as polyaniline (PANI)[12] and polypyrrole (PPy)[13-14]) or inorganic materials[15] have been reported, the capacitances and energy densities of assembled SCs were far from the practical application requirements due to the low loading mass of high-capacitance pseudo-capacitive active materials. It is still extremely challenging, especially in a solution environment, to achieve high loading mass of inorganic materials with a fine control over nanostructure on the CNTFs.

Pretreatment of CNTFs is an effective strategy to address the mentioned issue. On one hand, adjustable surface functional groups on each CNT facilitate loading of other pseudo-capacitive nanomaterials, which allows the textile conductor to act as both an active electrode and a current collector. Namely, it is a freestanding electrode, and a large enhancement in internal 3D space and surface wettability is expected to avoid the thickness limitation in flat film electrodes. On the other hand, transitional-metal oxides (e.g. MnO_2, Co_3O_4, NiO, and so on) suffer from unsatisfying cycling stability due to their low electrical conductivity. In recent years, experimental studies show that a substitution of O with S is an effective technique for overcoming the low electrical conductivity. In particular, ternary transition metal sulfides such as MCo_2S_4 (M = Ni[16-20], Cu[21-22], Mo[23], and Zn[24-26]) possess higher electrochemical activity and higher capacity than single-component sulfides based on richer redox reactions due to multiple oxidation states. Introducing sulfide vacancies has been demonstrated to be another effective route for improving the electrical conductivity of some transition metal sulfides because sulfide vacancies can act as shallow donors and thereby increase the carrier concentration. The co-existence of rich mixed valences of multi-metals and variable S benefits the formation of ionic defects (e.g., vacancies and misplaced ions) and electronic defects (electrons and holes), which is very promising for improving electrochemical performance. Nevertheless, the involved mechanisms are still unclear, and research on $Mn_xCo_yS_z$ with non-stoichiometry molar atomic ratios for SCs has not been reported yet. The effects of the non-stoichiometry, elements' atomic ratio, and enhanced electrical conduction on energy storage properties should be in-deep investigated.

In the present work, a freestanding, flexible high-performance $Mn_xCo_yS_z$/CNTF composite film electrode is developed via acid solution activation of dense CNTFs, growth of $Mn_xCo_y(CO_3)_{0.5}OH$ precursor, and controlled sulfidation. First, an effective acid solution activation strategy leads to an open-porous structure of CNTFs due to separation of adjacent NTs in 3D space, and also endows CNT surface with active groups for enhanced surface wettability. The activation transforms hydrophobic CNTF to be highly hydrophilic for facilitating uniform growth on each CNT assuring high loading percentages, and optimization of sulfidation leads to a nanoparticle-built porous coating. The electrochemical results show that optimal $MnCo_9S_{10}$/CNTF electrode has a specific capacitance of 450 F cm^{-3} at 10 mA cm^{-2}, and also exhibits remarkable cycling stability (only 1.6% capacity loss after 10,000 cycles) even at high current densities, much superior over previously reported values for similar CNT-based electrodes. The dependence of performance enhancement on the crystal structure and atomic ratio as well as the sulfide vacancies is comprehensively studied. Density-functional theory (DFT) calculation further confirms experimental results. An asymmetric flexible all-solid-state supercapacitor applying such electrode delivers volumetric energy density of 67 mW h cm^{-3} (at 10 W cm^{-3}). Integrated devices providing high output voltages were achieved by connecting several SCs and their potential application as an electric source was further proved. Particularly, there are no structural failure and performance loss during repeated folding and hammering.

2. Computational and Experimental Details

2.1 Computational Details. The first principles calculations based on the Density Functional Theory (DFT) were performed with spin-polarized generalized gradient approximation (GGA). Periodic DFT computations with the plane-wave pseudo-potential method as implemented in the program Vienna ab initio simulation package (VASP 5.4),[27] were carried out. All VASP calculations employed the generalized gradient approximation (GGA) with exchange and correlation treated by

Perdew−Burke−Enzerhoff (PBE).[28] The Monkhorst–Pack type of k-point sampling of $5\times5\times5$ was used and the plane-wave cutoff was set to 450 eV to strike a balance between accuracy and computational cost. The projector augmented wave (PAW) potentials were used to describe the electron−core interaction.[29,30] Spin polarization was considered here to calculate both the energies and structures.

2.2 Materials: Cobalt acetate tetrahydrate ($Co(CH_3COO)_2\cdot 4H_2O$), Urea ($CO(NH_2)_2$), concentrated hydrochloric acid (HCl, 35wt.%) and concentrated nitric acid (HNO_3, 65-67wt.%) were all bought from Sinopharm Chemical Reagent Co. Ltd. Manganese acetate tetrahydrate ($Mn(CH_3COO)_2\cdot 4H_2O$), and thioacetamide (CH_3CSNH_2, TAA) were all provided by Aladdin. All chemicals were analytical grade. Deionized water with a resistivity exceeding 18.0 MΩ cm from a JL-RO 100 Millipore-Q Plus purifier was used throughout the experiments.

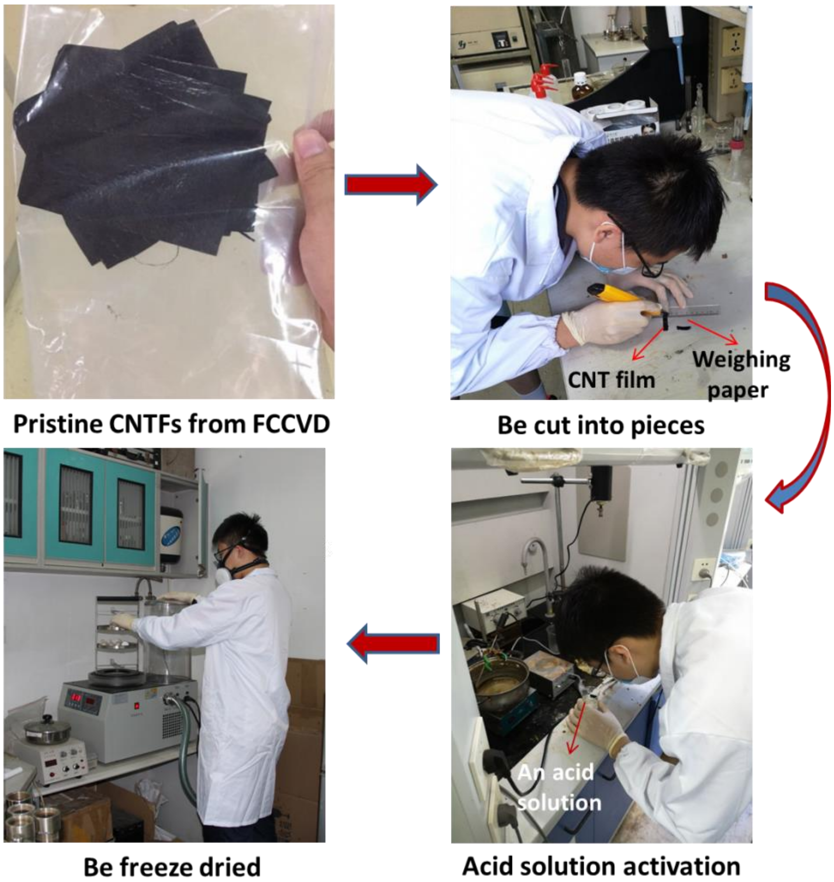

Figure 1. Typical photographs showing the acid solution activation process of the pristine CNTFs from the FCCVD method. The freeze drying is very important for remaining the enlarged networked structure of A-CNTFs.

2.3 Synthesis of Mn-Co Precursor@CNTFs: High-quality pristine CNTFs were prepared at 1300 ℃ using ethanol and ferrocene as carbon source and catalyst via a modified floating catalyst CVD (FCCVD) process. Then, the pristine CNTF from the FCCVD was cut into rectangular pieces with a size of 1 × 2 cm^2. Under continuous ultrasonic irradiation at a power of 100 W, the rectangular CNTF was soaked in 40 ml of 5wt.% aqueous HCl solution for a period of 30 min, and then was cleaned with deionized water. After that, the CNTF was soaked in a 20 ml of concentrated HNO_3 (65-67wt.%) for another period of different times. Finally the CNTF was cleaned by deionized water and freeze dried. Typical photographs showing the acid solution activation process of the pristine CNTFs are shown in **Figure 1**.

Figure 2. Typical photographs showing the procedure for hydrothermal preparation of precursor@CNTFs and the resulting Mn_xCo_yS@CNT composite films.

As for the synthesis of Mn-Co precursor@CNTFs, typically, a 40 ml water-ethanol (1:1 volume ratio) mixed solution of was prepared. Under a continuous stir, 0.2 mmol of cobalt acetate tetrahydrate and 0.1 mmol of manganese acetate tetrahydrate were dissolved in the mixture. Then, 0.06 g of urea was added under continuous stirring for 30 minutes. A piece of dried, activated CNTF (defined as A-CNTF) was soaked into the clear mixed solution, and transferred to a Teflon-lined autoclave with a volume of 50 mL. The autoclave was kept at a constant temperature of 140 ^{o}C in an oven for 3 h. The resulting Mn-Co precursor@CNT composite film was taken out, cleaned for several times with deionized water and isopropyl alcohol. Finally, the composite film was dried at 80 ^{o}C in air for 6 h.

2.4 Synthesis of $Mn_xCo_yS_z$@CNTF: The above-mentioned Mn-Co precursor@CNT composite film was immersed in 40 mL of ethanol containing 0.01 g TAA. The mixture was then transferred to a 50 mL Teflon-lined stainless steel autoclave. After being kept for 12 h at 120 ℃, the product was collected and washed. Finally, it was annealed at 350 ^{o}C in N_2 atmosphere for 2 h. Typical photographs showing the procedure for hydrothermal synthesis of precursor@CNT and the resulting $Mn_xCo_yS_z$@CNT composite films are shown in **Figure 2**.

2.5 Characterizations: The contacting angles of pristine CNTFs before and after the acid solution activation were measured by a dataphysics OCA-30 contact angle measurement system (the instrument is shown in **Figure 3**). The morphology of the CNTFs and composite films was investigated using scanning electron microscopy (SEM) (Hitachi S-4800 shown in **Figure 4**). X-ray diffraction (XRD) was carried out on a D/Max-RA X-ray diffractometer (Cu Kα = 1.5418 Å radiation) at 2^{o} min^{-1}. TEM, HRTEM, and SAED analyses were performed on a JEOL JEM-2100 electron microscope at an acceleration voltage of 200 kV. XPS was used to analyze the valence states of elements in a Thermo VG Scientific MultiLab ESCA2000 system with a CLAM4 hemispherical analyzer at a base pressure below 3 ×10^{-10} mbar. The quantity of the individual elements was analyzed by energy-dispersed X-ray spectroscopy (EDS). EDS analysis and elemental mappings were carried out on the same FESEM microscope. The EDS analysis was performed repeatedly via collecting information from a large area in a low-magnification SEM mode. Also, XPS measurements were performed at several different locations of one sample, and then the compositional ratios were averaged. The quantity of the individual elements was analyzed by inductively coupled plasma (ICP) on a J-A1100 ICP spectrometer (Jarrell-Ash Company, USA). 5 mg of the sample was dissolved in 10 ml of 4 M HNO_3 aqueous solution, and then diluted with deionized water to 100 ml. After that, 2 ml solution was taken and diluted to ppm level for subsequent ICP measurements. BET N_2 adsorption/desorption isotherms were measured at 77 K using a surface area analyzer (Micromeritics ASAP 2020) to investigate the surface characteristics. The samples were kept in vacuum at 323 K for 2 h to remove adsorbed gases before measurements. Specific surface areas and the pore-size distributions were determined using the Brunauer-Emmett-Teller (BET) and the BJH methods, respectively.

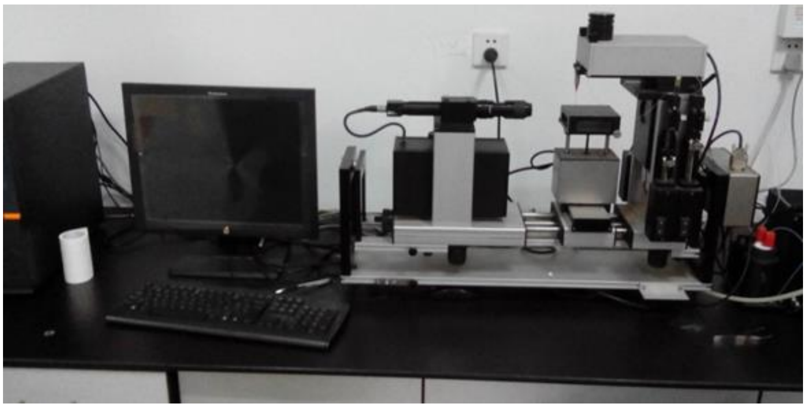

Figure 3. A data-physics OCA-30 contact angle measurement system for measuring the contacting angles of pristine CNTFs before and after the acid solution activation.

Scanning electron microscope (Hitachi S-4800)

XRD measurement on the X-ray diffractometer

Surface area analyzer (Micromeritics ASAP 2020)

Figure 4. A canning electron microscope (Hitachi S-4800) and a surface area analyzer (Micromeritics ASAP 2020) for BET measurements.

2.6 Electrochemical Measurements: Electrochemical measurements were carried out using a computer controlled Metrohm Autolab 302N electrochemical workstation (see **Figure 5**). For three-electrode tests, a platinum plate was served as the counter electrode and a standard Ag/AgCl electrode as reference, the $MnCo_9S_{10}$@CNTF was used as the working electrode, the effective area is 1 cm^2, leaving 1 cm for connection clamps. The electrolyte was 3 M KOH aqueous solution. CVs measurements were performed between -0.2 and 0.4 V (vs. Ag/AgCl). The specific capacitance (C_v) can be calculated from the GCD curves based on $C_v = I\,\Delta t\,/\,(V\,\Delta U)$, where i (A), Δt (s), V (cm^3), and ΔU (V) represent the discharge current, total discharge time, the volume of the whole electrodes, and potential window during discharge, respectively.

Metrohm Autolab 302N electrochemical workstation

Electrochemical measurements

Recording charge-discharge curves in a computer

Figure 5. A computer controlled Metrohm Autolab 302N electrochemical workstation. Photos of carrying out electrochemical measurements and recording charge-discharge curves on it.

2.7 Flexible All-Solid-State SCs. To assemble flexible all-solid-state SCs, a solid gel electrolyte film was prepared firstly. Typically, 1 g of KOH was poured into 18 ml of deionized water and 1.5 g of PVA powder was added. The mixture was then heated to 90 ^{o}C under stirring until it became clear. The solution was mechanically stirred slowly for 2 h at r.t. in order to eliminate bubbles. Finally, the solution was poured into a mold to obtain KOH-PVA gel membranes. The CNTF was used as the negative electrodes. The ~ 0.1 mm thick KOH-PVA gel membrane was sandwiched in between, the positive and negative electrode surface attached with a layer of PET film is used for fixed CNTFs and thus serves as a solid electrolyte.

To determine practically meaningful energy and power densities of a flexible solid-state SC, the total area/volume of the entire device including the electrodes, solid-state electrolyte, the separator, current collectors and packaging materials should be taken into consideration. The volumetric energy density (E_v) and power density (P_v) of flexible solid-state SCs can be calculated based on $E_v = (1/2)\ C_v\ (\Delta U)^2$ and $P_v = E_v / \Delta t$, where C_v is specific volume capacitance based on the total volume of the device. In order to get high output voltages, integrated devices were made by connecting several SCs in series, as shown in a photo of **Figure 6**.

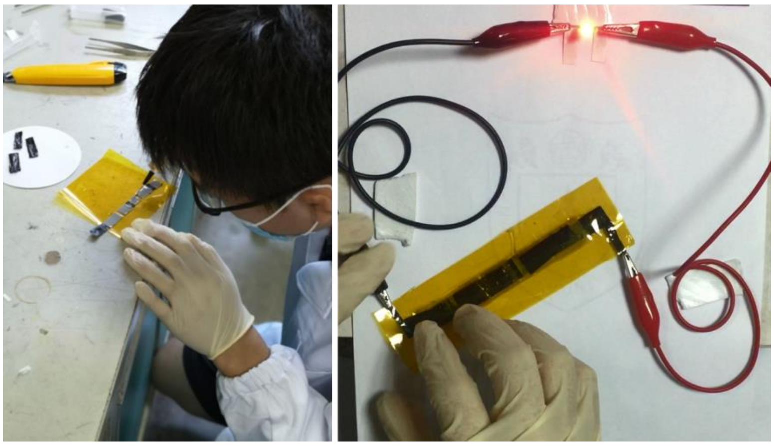

Figure 6. A photograph showing an assembly of all-solid-state SCs and connecting several of them into a single integrated device.

3. Results and Discussion

3.1 Theoretical Calculations

The first-principles calculations based on the DFT method are performed. **Figure 7** shows DFT theoretical calculation results of crystal structures. By replacing O atoms with S atoms, the O-O bond length changes from 2.713 Å for $MnCo_2O_4$ to 3.121 Å for the S-S bond length in $MnCo_2S_4$. The lattice cell parameter of $MnCo_2S_4$ is calculated to be $a = 9.347$ based on the DFT theoretical calculation, which is close to the value from XRD analysis ($a = 9.407$ Å from XRD peaks presented in the Ref.[31]). Also, the lattice cell parameter increases from 8.146 Å for $MnCo_2O_4$ to 9.347 Å for $MnCo_2S_4$, 15% increase in the lattice cell parameter (see **Table 1**). Such change is also observed in $ZnCoO_4$ system with 16% increase in bond length. In particular, the lattice cell parameter of $MnCo_9S_{10}$ is calculated to be 9.776 Å based on the DFT theoretical calculation. This implies that increasing the Co/S is helpful to enlarge the inter-atom bond length and hole size. In this work, the experimental and theoretical results for our synthesized $Mn_xCo_yS_z$ are both larger than that for $MnCo_2S_4$.

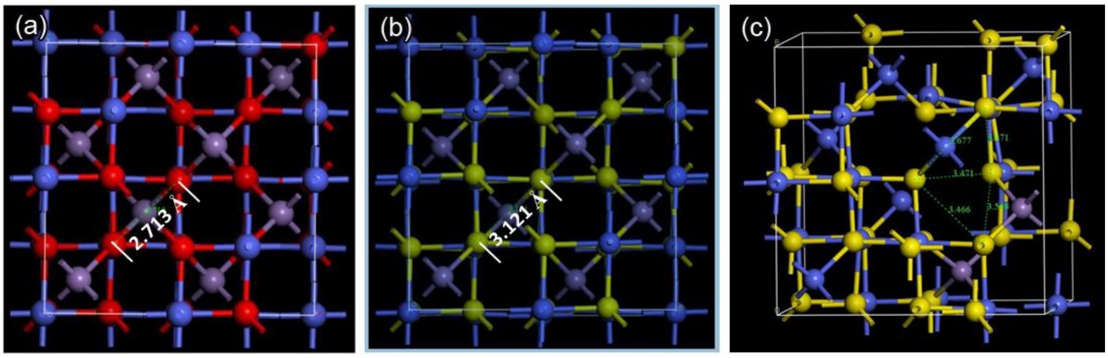

Figure 7. Theoretical calculation crystal structures through replacing O atoms with S atoms, from the first-principles calculations based on the DFT method. (a) $MnCo_2O_4$ from a unit cell, (b) $MnCo_2S_4$ from a unit cell, and (c) $MnCo_2S_4$ from a supercell.

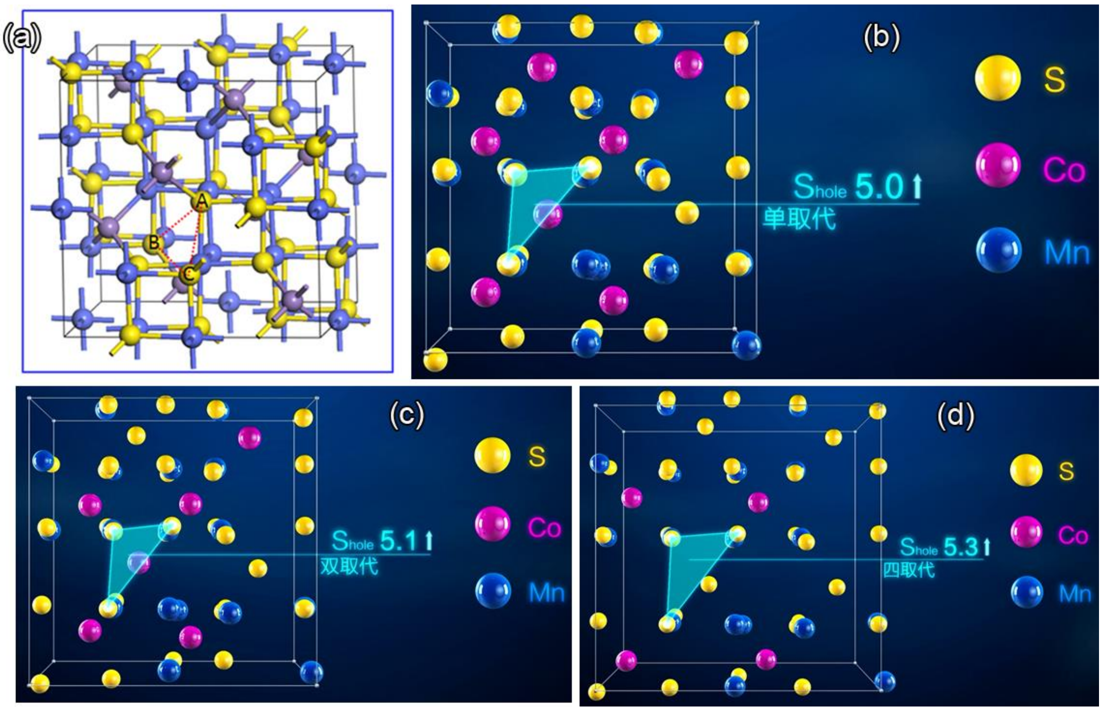

Figure 8. (a) Definition of a hole between three S atoms. The area (in red dashed lines, S_{hole}) can be obtained through Heron's formula. The area of holes after replacing Co with S atoms. (b) a One S atom is changed to Co in the supercell constructed via a 1×1×1 unit cell of optimized crystal structure of $MnCo_2S_4$. (c) Two S atoms are changed to Co. (d) Four S atoms are changed to Co.

The definition of a hole between three S atoms is presented in **Figure 8a**. The area (in red dashed lines, S_{hole}) can be obtained through Heron's formula: $S=\sqrt{p(p-a)(p-b)(p-c)}$, $p=\dfrac{a+b+c}{2}$, where a, b, and c, are the inter-atomic distances. Lower electronegativity of S than O leads to a more flexible structure through elongation between the layers, which has been confirmed by the DFT calculation results where the inter-atomic channel becomes larger and thus the volume of unit cell is enlarged when the O atoms in $MnCo_2O_4$ is replaced by S atoms.

Table 1. A comparison of lattice parameters and the area of holes

Crystal	Cell types	a (Å)	S_{hole} (Å^2)	Bond length (Å)
$MnCo_2O_4$	unit cell	**8.146**	**3.8**	**2.713**
$MnCo_2S_4$	unit cell	**9.347**	**4.9**	**3.121**
$MnCo_9S_{10}$[a]	supercell	**9.776**	**5.3**	**3.125**

[a] The supercell is constructed via a 1×1×1 unit cell of optimized crystal structure of $MnCo_2S_4$, followed by replacement of the corresponding atoms in the supercell.

Table 2. A comparison of lattice parameters and the area of holes

Crystal	Cell types	a (Å)	S_{hole} (Å^2)
$MnCo_2S_4$	unit cell	**9.347**	**4.9**
$MnCo_2S_4$[a]	supercell	**9.431**	**5.0**
$MnCo_2S_4$[b]	supercell	**9.441**	**5.1**
$MnCo_2S_4$[c]	supercell	**9.430**	**5.3**

[a] One S atom is changed to Co in the supercell constructed via a 1×1×1 unit cell of optimized crystal structure of $MnCo_2S_4$. [b] Two S atoms are changed to Co. [c] Four S atoms are changed to Co.

The influence of varying Co/S atomic ratio on crystal structure was further studied using the first-principles calculations based on the DFT method. **Figure 8b-d** shows DFT theoretical calculation results of crystal structures and the areas of holes after replacing Co with S atoms. As listed in **Table 2**, when only one S atom is changed to Co in the supercell, the lattice cell parameter increases to 9.431 Å. Interestingly, with a gradual increase of Co/S atomic ratio (more S atoms are changed to Co), the lattice cell parameter further increases to 9.441 Å but then reduces to 9.430 Å. The size of the holes increases gradually with the Co/S atomic ratio from 4.9 Å to 5.0 Å, 5.1 Å, and 5.3 Å. Taking $Mn_2Co_{19}S_{21}$ for example, the inter-atomic channel is further enlarged with the S-S bond length being 3.33 Å (9.436 × 9.436 × 9.436). Thus, increasing the concentration of Co in the unit cell can enlarge the size of the holes. This means that adjusting the Mn/Co atomic ratio can further enlarge the inter-atomic channels, which is beneficial for ultrafast ion diffusion. The obvious change in inter-atomic channel is because of taking advantage of the improved charge transfer due to energy difference between O2*p* and S2*p* levels. Although an optimal Co/S ratio for the largest S_{hole} size was not obtained, the above calculated results indicate that synthesizing a novel $Mn_xCo_yS_y$ with relatively higher Co/S atomic ratio is more favorable for the electron and ion transfer kinetics comparing with $MnCo_2S_4$.

3.2 Presentation of the Formation Process

The preparation process of $Mn_xCo_yS_z$/CNTF composite film electrode is schematically illustrated in **Figure 9**. The synthesis includes three main steps. A surface activation pre-treatment using acid aqueous solutions (the step I) plays a vital role for subsequent growth of Mn-Co precursor on each CNT. Without the activation, only the upper surface of whole pristine CNTFs is covered by a dense precursor layer, and those individual NTs in the interior of the CNTFs cannot be coated due to an inaccessibility of ions. Instead, through a activation treatment, the dense-packed pristine CNT films are converted to hydrogel-like ones that have greatly enlarged internal space and largely enhanced surface wettability. The pre-treatment activation process includes immersing the pristine CNT films in diluted HCl aqueous solution (5 wt.%) and concentrated HNO_3 (65 wt.%) one after another. Interestingly, the use of either HCl or HNO_3 cannot obtains the same result, and no obvious size change of a film is observed when only diluted HCl aqueous solution is used for activation. After immersing in HCl solution, the conductivity of the CNTF is increased due to removal of residual inorganic ferrocene catalyst. And concentrated HNO_3 oxidizes the surface of individual CNTs in CNTFs sufficiently and endows their surface with many active groups like hydroxyl, carbonyl, and carboxyl. The groups activated surface helps to generate repulsive force to expand the dense CNT network leading to an open-porous structure due to well-separation of adjacent NTs, and also transforms hydrophobic CNTF to be highly hydrophilic. After that, Mn-Co precursor grows on each nanotube in the activated CNTFs (A-CNTFs). At the beginning, the cations of Co^{2+}, Ni^{2+}, and NH_4^+ react with the CO_3^{2-} and OH^- anions released from a slow hydrolysis of urea, which leads to the precursor of $Mn_xCo_y(CO_3)_{0.5}OH$.[32] The active groups serve as nucleation centers for the subsequent uniform surface growth (the step II). The open-porous structure and greatly improved wettability/activity facilitate ions accessibility, which assures a ultra-high loading mass. In the step III (see the right part of the scheme), a $Mn_xCo_yS_z$ coating was obtained after sulfidation of the Mn-Co precursor. The possible chemical reaction equations are as follows:

$$\mathrm{CO(NH_2)_2 + H_2O \rightarrow CO_3^{2-} + 2NH_4^+} \tag{1}$$

$$\mathrm{Mn(CH_3COO)_2 + Co(CH_3COO)_2 \rightarrow Mn^{2+} + Co^{2+} + 4CH_3COO^-} \tag{2}$$

$$\mathrm{CH_3COO^- + H_2O \rightarrow CH_3COOH + OH^-} \tag{3}$$

$$\mathrm{xMn^{2+} + yCo^{2+} + 0.5CO_3^{2-} + (2z-1)OH^- \rightarrow Mn_xCo_y(CO_3)_{0.5}(OH)_{2z-1}} \tag{4}$$

$$\mathrm{CH_3CSNH_2 + H_2O \rightarrow CH_3CONH_2 + H_2S} \tag{5}$$

$$\mathrm{Mn_xCo_y(CO_3)_{0.5}(OH)_{2z-1} + zH_2S \rightarrow Mn_xCo_yS_z + 2zH_2O + CO_2} \tag{6}$$

Optimization of sulfidation reactions leads to a nanoparticle-built nanoporous coating. The anion-exchange rate is determined by the concentration of TAA (defined as C_{TAA}), and thus controlled sulfidation is also important for the nanostructure modulation. A relatively low C_{TAA} is necessary for sulfidation. Optimization of the C_{TAA} leads to a nanoporous $\mathrm{MnCo_xS_y}$ coating. Nanoparticle-built porous coatings are achieved at relatively slow reactions ($C_{\mathrm{TAA}} \leqq 20$ mM) while dense and smooth coatings are formed instead at $C_{\mathrm{TAA}} > 20$ mM where the anion-exchange rate is relatively high. The former is desirable for SCs' electrode materials due to its larger porosity as well as providing much more active sites. Experimental demonstration of specific nanostructure dependence on the C_{TAA} will be further discussed in detail later.

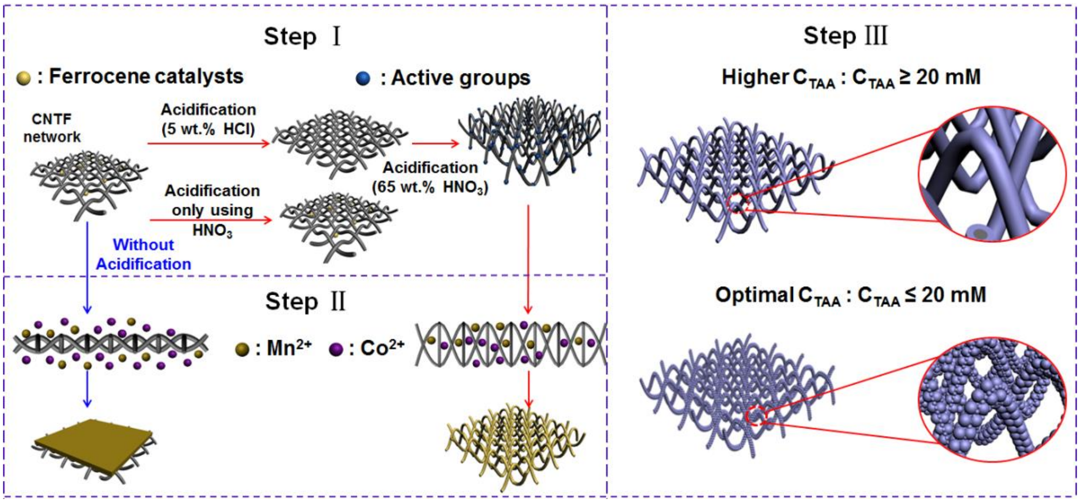

Figure 9. Schematic illustration of the formation of $Mn_xCo_yS_z$@CNTFs composite electrode. The synthesis includes the activation of pristine CNTF using diluted HCl (5 wt.%) and concentrated HNO_3 one after another (the step I), precursor growth (the step II), and controlled sulfidation (the step III). A direct growth of precursor leads to a dense surface layer on the whole film.

3.3 Morphology and Nanostructure Characterizations

Figure 10a shows a digital photograph of a pristine CNT film synthesized from a floating catalyst CVD (FCCVD) method before (the upper half) and after (the lower half) activation pre-treatment. The large film was cut into a rectangular shape (4 cm length × 2 cm width). Obviously, after two-step activation treatment of a half of a CNTF, the width of the rectangular film increases from 2 cm to 2.3 cm, with 15% size increment. **Figure 10b** and **10c** show the cross-section SEM images of a pristine CNT film before and after activation. The internal space is highly enlarged, as confirmed by the film thickness increase from 9.5 μm to 263.5 μm. An obvious increase in both the width and the thickness indicates that a CNT film expands in three-dimensional space. Interestingly, the size increases in the width (15%) and thickness (27 times) are much different. This is because a film consists of ultra-long CNTs that are inter-crossed in the 2D space. Namely, when it is expanded remarkably in volume, individual CNT is getting straight from bending while the adjacent CNTs along the direction perpendicular to film are separated from each other. The pristine CNT film has an excellent mechanical strength reaching around 30~50 MPa, and the mechanical strength can be remained. Before the activation treatment, the pristine CNTF is hydrophobic and its surface cannot be wetted by water, but the activated films showed greatly improved surface wettability. The surface contacting angle changes from 120° before activation (**Figure 10d**) to 60° after activation (**Figure 10e**), which indicates that the activation pretreatment transforms the hydrophobic CNTNF to be highly hydrophilic. This is mainly attributed to both the presence of active groups on CNT surface and the network nanostructure change. The obvious volume expansion of CNTF is attributed to the well-separation of adjacent NTs, which is further confirmed by scanning electron microscopy (SEM) observation. In the pristine CNTF, individual CNTs attach to each other and they prefer to exist in thick bundles (**Figure 10f**). Its dense network structure and hydrophobic surface undoubtedly blocked ions from efficient diffusion throughout the film, which leads to that it is similar to a planar substrate. After activation, adjacent CNTs become well separated to form into 3D network (**Figure 10g**), as is confirmed by a high BET surface area of 276 m^2 g^{-1}. The mass density of the pristine CNTF greatly reduces from being ~ 100 mg cm^{-3} to 2000 mg cm^{-3} due to ~20 times enlargement in the volume. The volume expansion provides large internal space combined with active groups on each nanotube surface, which facilitates subsequent anchoring of Mn-Co precursor.

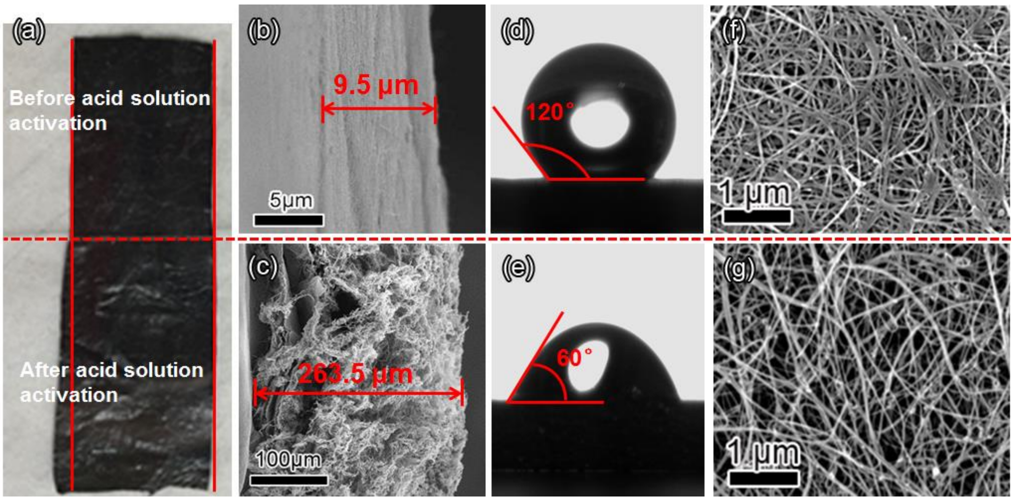

Figure 10. Detailed comparisons of a CNT film before and after activation. (a) A digital photograph of a pristine CNT film synthesized from FCCVD before (the upper half) and after (the lower half) activation. (b, c) Cross-section SEM images of the film and (d, e) contacting angles recorded from the CNTF surface, and (f, g) the corresponding SEM images.

By adjusting the molar ratio of Mn^{2+}/Co^{2+} in the mixed reaction solutions and subsequent sulfidation, high Co/S atomic ratios in the resulting $Mn_xCo_yS_z$ were obtained. **Figure 11**a shows a low-magnification SEM image of typical $Mn_xCo_yS_z$/CNTF composite film. The film is composed of ultra-long $Mn_xCo_yS_z$ coated CNTs with lengths reaching tens of micrometers resulting in a loosely porous microstructure. The original uniform 3D network nanostructure of the pristine CNTF is inherited, and each CNT has a uniform surface coating without other by-products. As shown in a magnified SEM image (**Figure 11b**), the resulting $Mn_xCo_yS_z$ coated CNTs look uniform with an average diameter being roughly 250 nm. Comparing to the precursor coated CNTs (the inset of **Figure 11b**), the $Mn_xCo_yS_z$/CNTs have rougher surfaces, and there is 50 nm increase in diameter. A magnified SEM image showing a single tube (**Figure 11c**) indicates that the $Mn_xCo_yS_z$ coating consists of a large number of nanoparticles of ~20 nm in diameter that form a loosely-packed porous surface. A TEM image **(Figure 11d**) reveals that each CNT is coated by the loose $Mn_xCo_yS_z$ coating where hollow interior of CNTs and rough coating with many nanopores are both visible. The pristine bare CNT (before coating) is multi-walled with outer diameter around 40 nm, as shown in the TEM image (inset of **Figure 11d**). Thus, the thickness of $Mn_xCo_yS_z$ nanoparticle-built porous coating is about 100 nm. The porosity of the coating can be further demonstrated by a high BET surface area of 416.34 $m^2 g^{-1}$ (**Figure 11e**) and the BJH adsorption average pore-diameter distribution (see the inset) in a narrow range of 3~7 nm. The $Mn_xCo_yS_z$ is tightly bound with individual CNTs, presenting a robust and stable hybrid structure.

As mentioned above, high mass loading is very important for obtaining enhanced capacitances. In order to measure the loading mass of $Mn_xCo_yS_z$ in the composite film, thermogravimetric analysis (TGA) was performed. The TGA curve (**Figure 11f**, on the left) shows a first weight fluctuation at about 280~500 (DTG-peak) even a slight increase of mass is observed, which is because lightweight sample floats as the temperature rises. After that point, the continuous weight loss from 520 to 670 ^{o}C originates from the combustion of CNTF. When the temperature is higher than 670^{o}C, no weight loss happens. According to the weight loss, the loading percentage of

$Mn_xCo_yS_z$ in a typical composite film is calculated to be 67.7 wt%. This value is close to that calculated from the weight change before and after coating (69.5 wt.%). In the differential scanning calorimetry (DSC) heat flow plots (**Figure 11f**, on the right), a strong exothermic peak at around 600 ^{o}C is due to combustion of CNTF. Our method assures a high loading mass of grown active materials ($Mn_xCo_yS_z$) up to ~80 wt.%, which is higher than reported results in the literature.[10, 31]

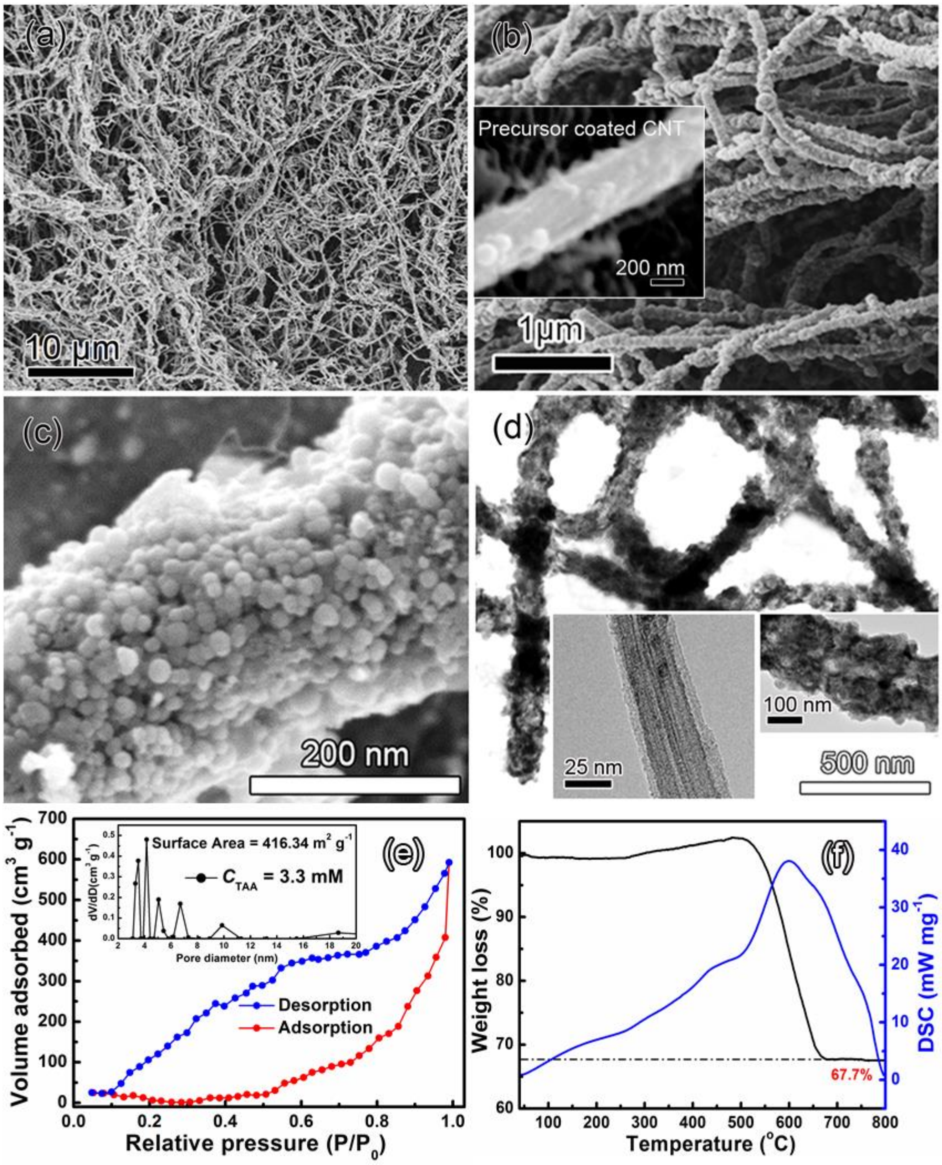

Figure 11. Detailed characterizations of the typical $MnCo_9S_{10}$ coated CNTs composite film. (a-c) SEM at different magnifications, and (d) TEM image of several $MnCo_9S_{10}$ coated CNTs from the composite film. The inset of (b) is the precursor coated CNTs, and the inset of (d) is a TEM image of a single bare CNT (on the left) and a single $Mn_xCo_yS_z$ coated CNT (on the right). (e) BET results with the inset showing BJH average pore-diameter distribution. (f) TG and DSC curves.

Figure 12a shows the X-ray diffraction (XRD) patterns of pristine CNTF (the black curve) and the resulting $Mn_xCo_yS_z$/CNTF (the blue curve). A broad peak at around 26.6^o is associated to the carbon. The 2θ scan's peaks at 31.7^o, 35.62^o, 38.5^o, 54.2^o, and 58.8^o should correspond to the (200), (210), (211), (311), and (230) crystal planes of $Mn_xCo_yS_z$, respectively. Although there is a slight shift towards the smaller degrees, these peaks are all close to those for $MnCo_2S_4$ (black lines for standard peaks' positions). The shift of diffraction peaks should be attributed to the difference in crystal structure originated from varying Mn/Co/S atomic ratio. Based on the XRD peaks, the lattice cell parameter of $Mn_xCo_yS_z$ is calculated to be 9.723 Å, which is larger than that for $MnCo_2S_4$ (a = 9.407 Å from XRD peaks presented in the Ref.[32]). In particular, the value of 9.723 Å from the XRD peaks is also close to result from the theoretical calculation. Therefore, the experimental results are in good agreement with those from our theoretical calculation.

X-ray elemental mappings recorded from a single $Mn_xCo_yS_z$/CNT (**Figure 12b**) reveal that different elements of Co (green), S (red), and Mn (cyan) are homogeneously distributed along with the whole tube, which implies a uniform coverage of the CNT by $Mn_xCo_yS_z$ compounds. Obviously, the Co element has a relatively high atomic percentage comparing with Mn element. EDS results show elements' characteristic peaks, and atomic percentages of Mn, Co, and S are 5.1, 44.8 and 50.1 at.%, respectively (data listed in the inset). Their atomic molar ratio is thus 1: 8.79:9.82 (about 1: 9: 10). This was further corroborated by inductively coupled plasma (ICP) analysis result (see **Table 3** below) where the weight percentages of Mn, Co and S elements are 6.15 wt.%, 56.68 wt.%, and 37.18 wt.%, respectively. The Mn: Co: S atomic ratio is thus 0.05: 0.43: 0.52 (1 : 8.60: 10.40).

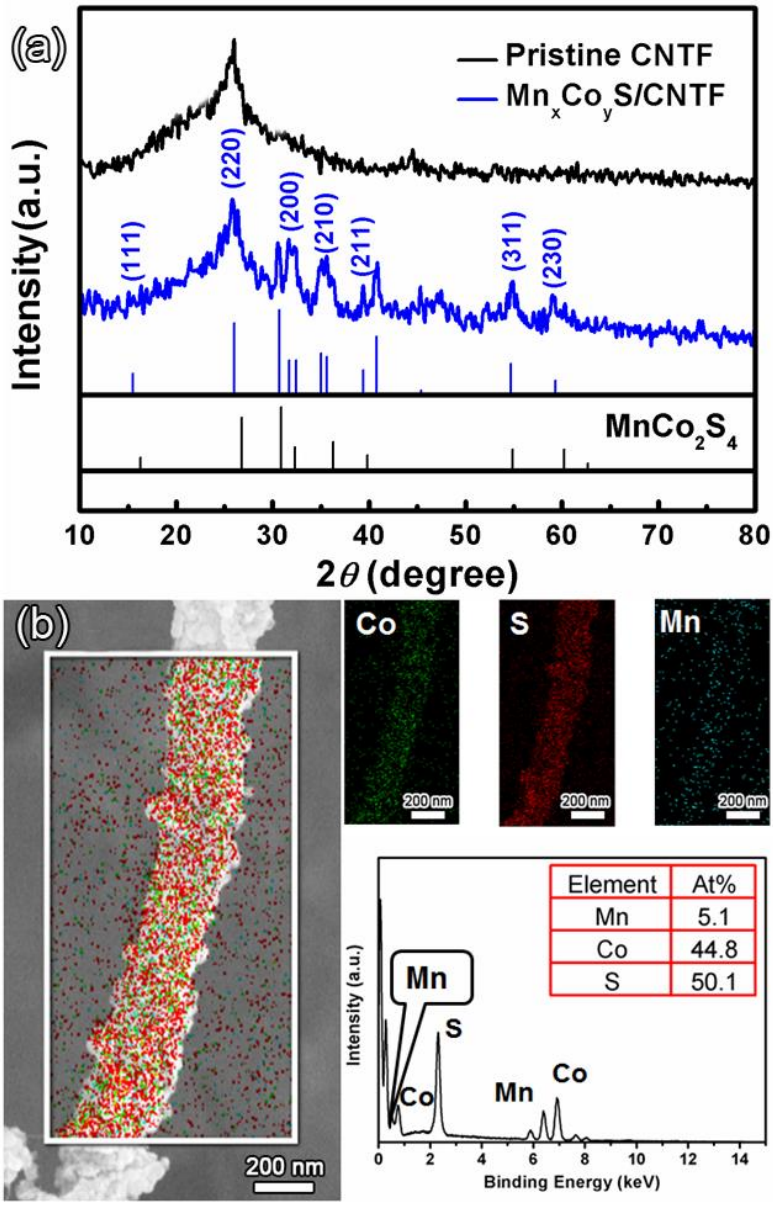

Element	At%
Mn	5.1
Co	44.8
S	50.1

Figure 12. (a) XRD patterns of pristine CNTF and the resulting Mn$_x$Co$_y$S$_z$/CNTF. (b) A SEM image (on the left) with X-ray elemental mappings recorded from a single CNT coated with Mn$_x$Co$_y$S$_z$ (the upper right images), EDS spectrum with the elementals' atomic percentages (the lower right spectrum).

The oxidation states of these elements are further evaluated by X-ray photoelectron spectroscopy (XPS). The survey (**Figure 13a**) demonstrates the main presence of Mn, Co, and S elements. By using Gaussian fitting, two types of manganese species were observed in the Mn2*p* spectrum (**Figure 13b**), which are ascribed to the presence of mixed Mn^{4+} and Mn^{3+}. The peaks located at 641.6 and 653.9 eV are ascribed to Mn^{4+} and those at 642.8 and 654.9 eV should be related to

Mn^{3+}.[33] From the Co2*p* spectrum (**Figure 13c**), two distinct peaks with binding energies of 781.4 and 797.4 eV correspond to the Co2*p*3/2 and Co2*p*1/2 with two satellite peaks at 785.4 and 803.4 eV, which are the characteristic peaks of Co^{2+}. The peak at 781.4 eV could be ascribed to a Co oxidation state, and two peaks at 778.9 and 794.0 eV are assigned to Co^{3+}. The binding energy of 778.9 eV is slightly higher than that of metallic cobalt (778.0 eV), indicating that the Co carries a partially positive charge (Co$^{\delta+}$). In the S2*p* spectrum (**Figure 13d**), the main peaks at 162.0 and 163.0 eV belong to S2*p*3/2 and S2*p*1/2, respectively, the typical characteristic of S_n^{2-} with metal ions (Co-S_n and Mn-S_n bonding). The slight shift of the peaks reveals the presence of S vacancies, which might be from the non-stoichiometry. Therefore, the coexistence of rich-mixed valence states (Co^{3+} and Co^{2+}), (Mn^{3+} and Mn^{4+}), and S vacancies for the Mn, Co and S elements is demonstrated. According to the XPS analysis, atomic molar ratio of Mn, Co, and S is 2.16%:18.4%: 20.9% (1:8.52:9.68).

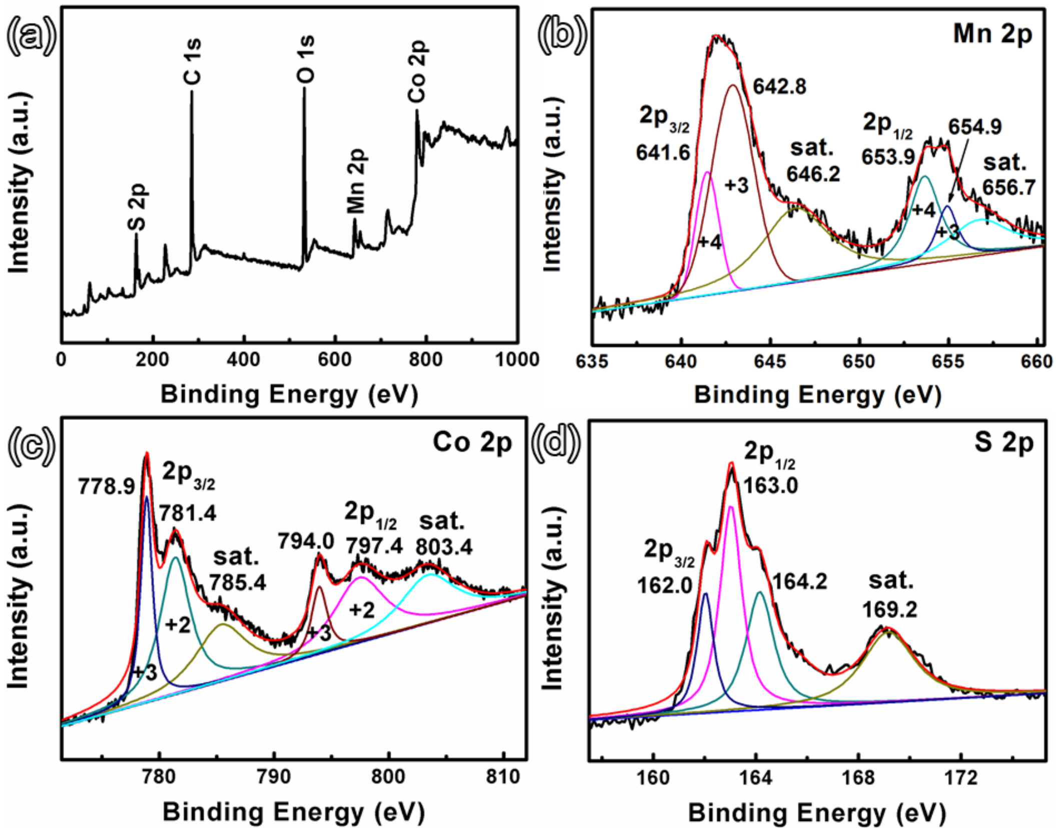

Figure 13. (a) XPS survey, and high resolution XPS spectra of (b) Mn 2*p*, (c) Co 2*p*, (d) S 2*p* characteristic peaks recorded from the $Mn_xCo_yS_z$/CNTF.

Table 3. Composition results of our $Mn_xCo_yS_z$/CNTF product by different quantitive analysis methods including ICP, EDS, and XPS.

Analytical method	Measured Mn: Co: S atomic ratio
EDS	5.1 : 44.8 : 50.1 (1 : 8.79 : 9.82)
XPS	2.16: 18.4: 20.9 (1 : 8.52 : 9.68)
ICP	0.05:0.43:0.52 (1 :8.60: 10.40)

As summarized in Table 3, the Mn:Co:S atomic molar ratios from the XPS and ICP measurements are both consistent with the EDS result (about 1:9:10). Therefore, the composition of the coating is suggested to be $MnCo_9S_{10}$. Interestingly, the atomic molar ratio is not consistent with the used reactants' stoichiometry ($n_{Mn}{}^{2+}/n_{Co}{}^{2+} = 1:2$). This maybe attributed to that Co^{2+} ions are easier to combine with $CO_3{}^{2-}$ and OH^- (see the equation 4) comparing with Mn^{2+}, which results in a much higher atomic percentage of Co in the precursor and the resulting sulfides.

As discussed above, the activation with concentrated HNO_3 (after immersion in HCl solution) plays a decisive role for the volume expansion of CNTF network films in 3D space. **Figure 14**a compares electrochemical impedance spectroscopy (EIS) curves of the CNTs after activation with different immersion time of concentrated HNO_3 (defined as t_{HNO3}). R_{ct} is the Faradic charge-transfer resistance (semicircle at high frequencies) and R_e is the bulk resistance of the system including electrolyte and internal resistance of the electrode. After activation with a short time, the resistances are still high because of a small change comparing with the pristine CNTF. With an increase of t_{HNO3}, R_{ct} and R_e both increase initially and then decline. Among the composite films, the $MnCo_9S_{10}$/CNT obtained with t_{HNO3} = 6 h has the smallest resistances ($R_{ct} = 1.51\ \Omega$, $R_e = 0.15\ \Omega$). This further indicates that the optimal t_{HNO3} = 6 h leads to the highest electrical conductivity. The impedance of CNTFs mainly comes from the contact resistance between the adjacent CNTs. After coating, the CNT-CNT contact is replaced by the conductive $MnCo_9S_{10}$. The electron/ion transfer is accelerated, which effectively reduces internal resistance of the whole film system.

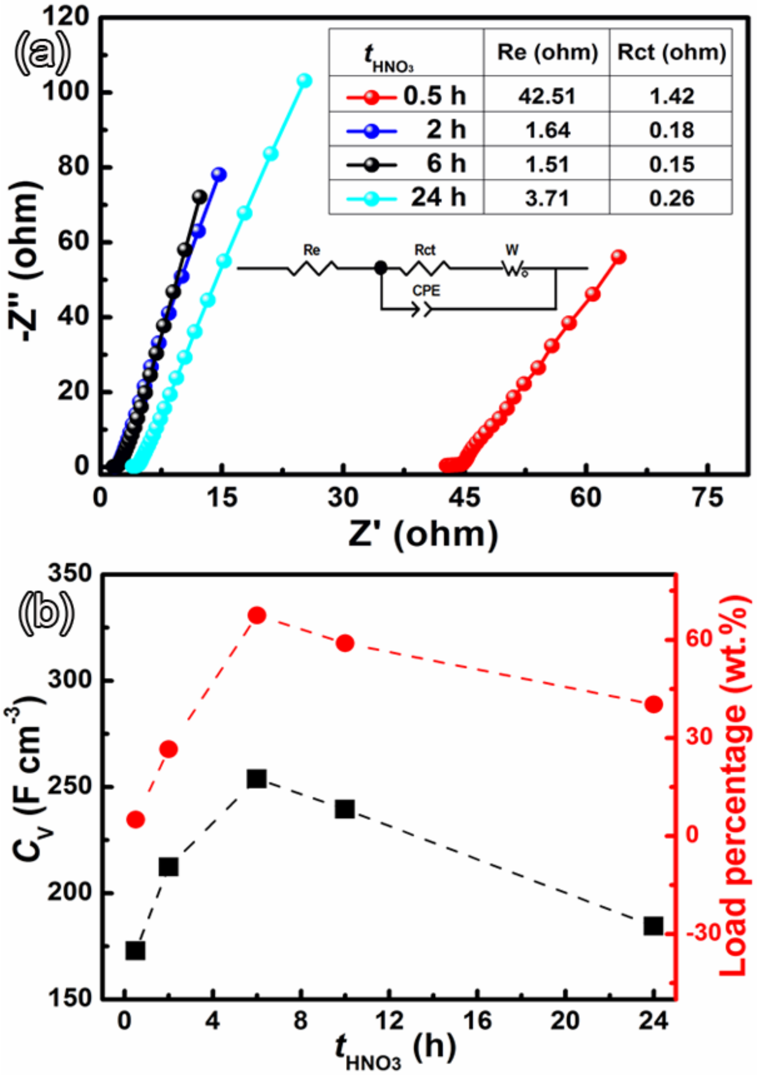

Figure 14. (a) EIS curves of the pristine CNTFs after activation for different t_{HNO3}; the inset shows the equivalent circuit and the corresponding R_e and R_{ct} values. (b) loading percentages of $MnCo_9S_{10}$ and specific volume capacitances of the resulting $MnCo_9S_{10}$/CNTF vs. the t_{HNO3}.

The loading percentages of $MnCo_9S_{10}$ with varying t_{HNO3} is shown in the red curve of **Figure 14b**. After a relatively short t_{HNO3}, $MnCo_9S_{10}$ nanoparticles with a sparse distribution form on single CNT's surface. With a gradual increase of t_{HNO3}, the loading percentage of $MnCo_9S_{10}$ increases firstly and then declines, it reaches the highest value being 66 wt.% at t_{HNO3} = 6 h. It turns out that longer t_{HNO3} doesn't help to increase the loading percentage of active materials. This is because newly formed Mn-Co precursor cannot grow on the surface of individual CNTs but in the solution instead. Also, specific volume capacitance of the resulting composite films is maximized at this point (t_{HNO3} = 6 h), as shown in the black curve of **Figure 14**b. The change trend in the red and black curves is the same. Obviously, the increase rate (slope of curve) is different in two separate stages. When $t_{HNO3} \leq 6$ h, the load percentages of $MnCo_9S_{10}$ and specific capacitance both increase rapidly (the slop is steeper), which indicates that the volume expansion of CNTF is large at the initial stage. In spite of a large volume expansion, the mechanical stability even the structural integrity of CNTF is remained. Based on the results, $t_{HNO3} = 6$ h is the optimal time considering structure integrity and uniformity of the films, high loading percentages of $MnCo_9S_{10}$, electrical conductivity, and specific capacitance.

As is known that electrochemical performance depends on the nanostructure of electrode materials and high specific surface area is thus desirable. It is found that the porosity of the $MnCo_9S_{10}$ coating can be controllable by the C_{TAA} that determines the anion-exchange reaction rate. With a gradual decrease of C_{TAA}, specific BET surface area increases initially then declines, and reaches the largest at $C_{TAA} = 0.03$ mM (**Figure 15**a). This indicates that a relatively low C_{TAA} is necessary for obtaining porous coating. As seen from the BJH adsorption average pore-diameter distribution (the insets of **Figures 15a-c** and **11e**), when the C_{TAA} is smaller than 20 mM, all the coatings exhibit nano-pores; the pore diameters in the coatings obtained at lower C_{TAA} are relatively large. At the optimal C_{TAA} of 0.03 mM, nanoparticle-bulit porous coatings on individual CNTs are achieved while dense and smooth ones are formed instead at higher C_{TAA} than 20 mM where the anion-exchange rate is too high. More importantly, specific capacitance is also optimized at that point ($C_{TAA} = 0.03$ mM), which further confirms the nanostructure optimization.

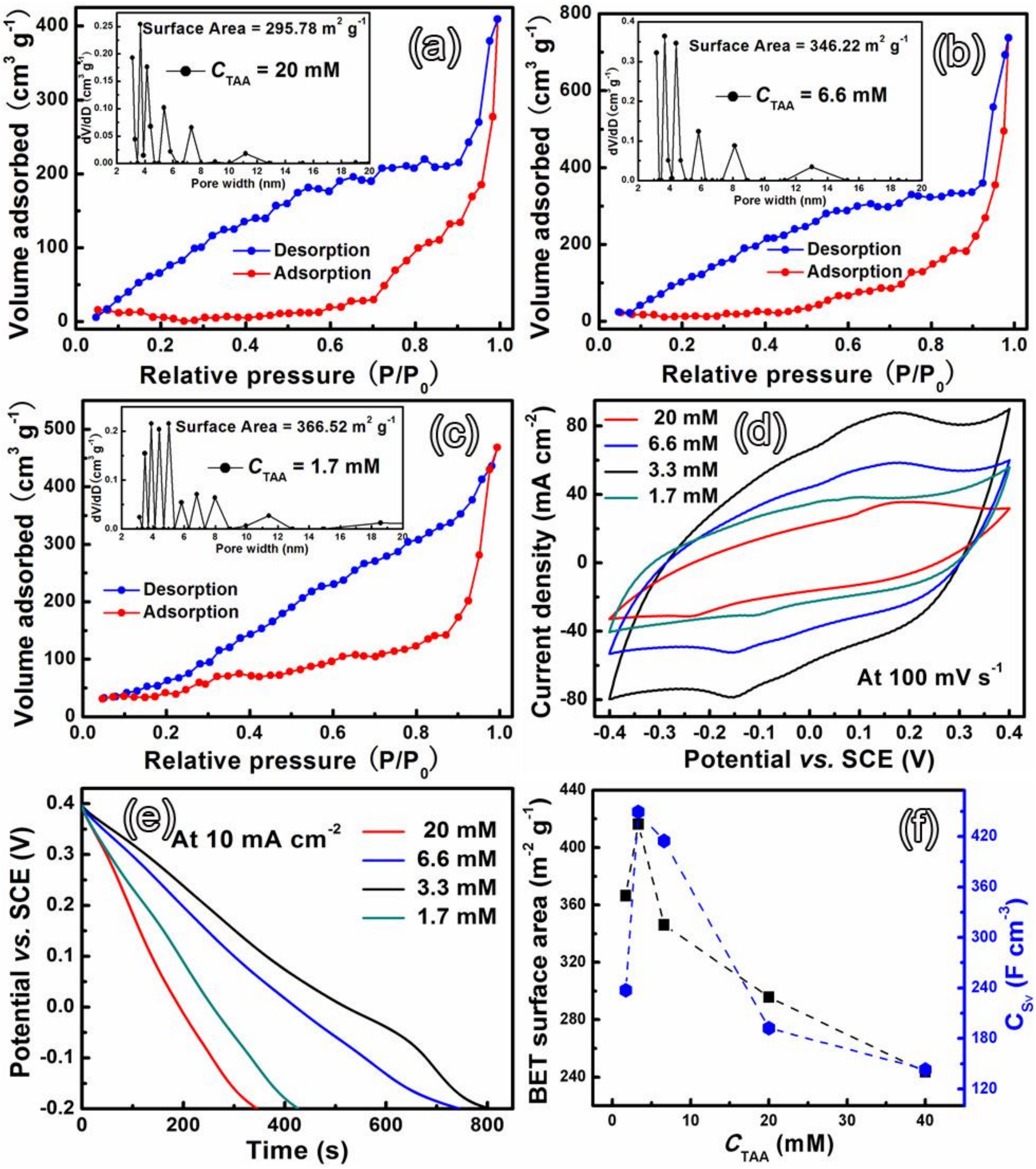

Figure 15. BET results showing surface area of the resulting $Mn_xCo_yS_z$/CNTF obtained with different C_{TAA} of (a) 20 mM, (b) 6.6 mM, and (c) 1.7 mM. Insets are the corresponding BJH adsorption average pore-diameter distributions. (d) CV curves at 100 mV s^{-1} and (e) Discharge curves at 10 mA cm^{-2} of the $Mn_xCo_yS_z$/CNTF obtained with different C_{TAA}. (f) Curves showing the change of measured BET surface areas and specific volume capacitances with C_{TAA}.

3.4 Electrochemical Performance

As shown in the cyclic voltammetry (CV) curves of the products obtained with different C_{TAA} (**Figure 15d**), the presence of redox peaks corresponding to the reversible faradaic reactions of $MnCo_9S_{10}$ indicates its battery-type electrochemical behavior. Also, the near-rectangular shape of the CV curves indicates a pseudo-capacitive behavior. At a given scan rate of 100 mV s^{-1}, the largest area circled in the CV curve of the $MnCo_9S_{10}$/CNT obtained with C_{TAA} = 3.3 mM (the black curve) indicates the highest capacitance. The redox peaks are originated from the equations (7-9). **Figure 15e** shows GCD curves of the $MnCo_9S_{10}$/CNTF obtained from different C_{TAA}. The good symmetry reveals a reversible charge-discharge behavior. At a current density of 10 mA cm^{-2}, a gradual reduction of C_{TAA} leads to that the black discharge curve (C_{TAA} = 3.3 mM) shows the longest discharge time (**Figure 15f**), which is related to the C_{TAA} dependent specific nanostructure. Based on these results, the porosity of the $MnCo_9S_{10}$ coating and the specific capacitance are both optimized at C_{TAA} = 3.3 mM.

It is reported that the reversible redox reactions of $NiCo_2S_4$ give rise to the formation of CoSOH and NiSOH.[7, 20] $Mn_xCo_yS_z$ is similar to $NiCo_2S_4$, thus it is believed that its energy storage mechanism in alkaline electrolyte should be via reversible redox reaction of $Mn_xCo_yS_z$ to form Mn_xSOH, Co_ySOH, $Mn_xS_{z-1}O$ and Co_ySO, which can also be demonstrated by the presence of two pairs of relatively inapparent redox peaks in the red CV curves. The reversible redox reactions during the charge and discharge processes are schematically illustrated in **Figure 16.** The possible reaction equations could be expressed as follows:

$$Mn_xCo_yS_z + 2OH^- \leftrightarrow Mn_xS_{z-1}OH + Co_ySOH + 2e^- \qquad (7)$$

$$Mn_xS_{z-1}OH + OH^- \leftrightarrow Mn_xS_{z-1}O + H_2O + e^- \qquad (8)$$

$$Co_ySOH + OH^- \leftrightarrow Co_ySO + H_2O + e^- \qquad (9)$$

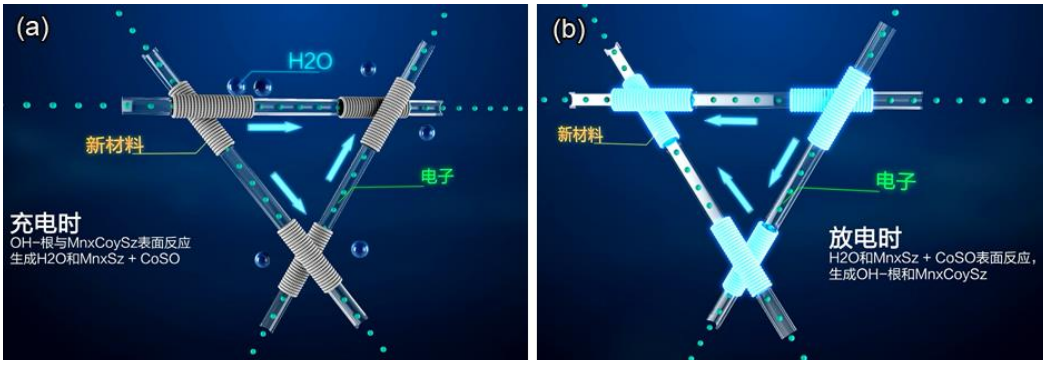

Figure 16. Schematic illustration of the reversible redox reactions between the active electrode materials and the electrolyte.

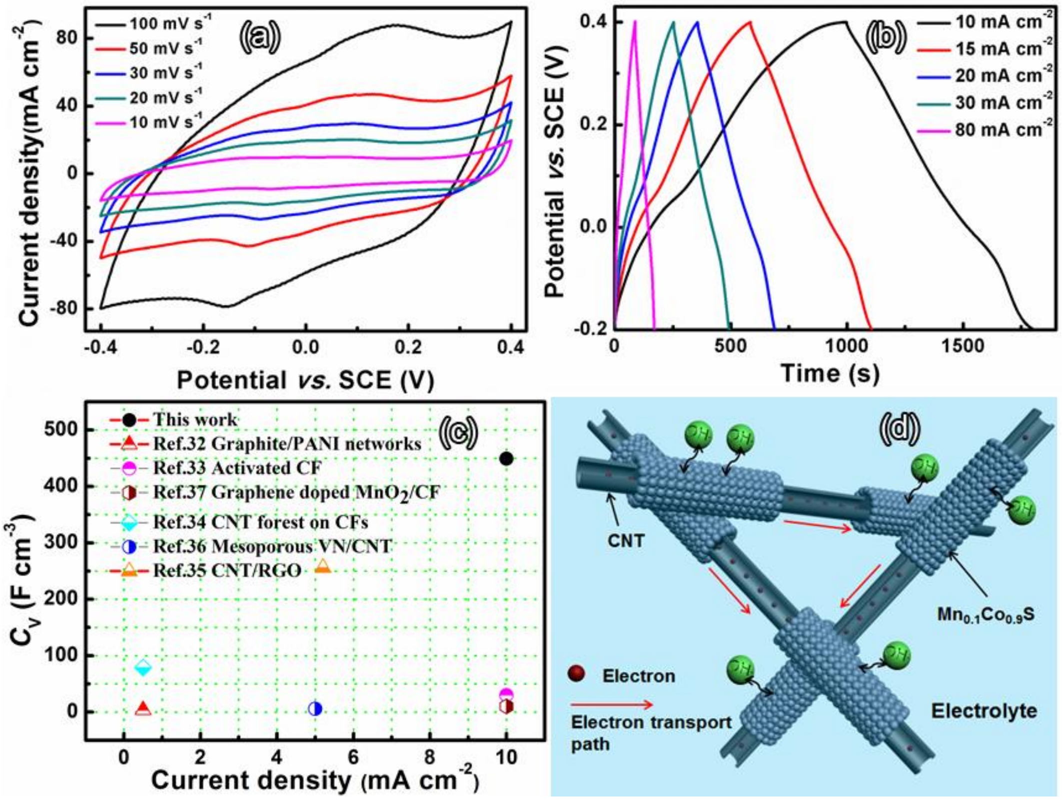

Figure 17. (a) CV curves at various scan rates, and (b) galvanostatic charge-discharge (GCD) curves at different current densities of the $MnCo_9S_{10}$/CNTF electrode. (c) The specific capacitance vs. current density, a capacitance comparison with other similar CNT or carbon-based composite films. (d) Schematic illustration of 3D network with the largely opened geometry facilitating the electron transfer and OH^- ion diffusion.

Figure 17a shows CV curves of the optimal $MnCo_9S_{10}$/CNTF electrode at various scan rates. The curves' area increases with the scan rate, consistent with ternary transition metal sulfides presented in the literature. **Figure 17**b shows GCD curves of the electrode at various current densities. Based on the discharge curves, the corresponding specific volume capacitances are calculated to be 449, 437, 403, 398, 391 and 370 F cm^{-3} at 10, 15, 20, 30, 50 and 80 mA cm^{-2}, respectively. The C_v value of 449 F cm^{-3} (at 10 mA cm^{-2}) is much higher than those of recently reported similar electrode materials of CNT or carbon fiber (CF) based composites, such as bamboo-like O-doped porous CNTs[35] (data are listed in **Table 4**).

Table 4. Electrochemical performance comparison of our optimized $MnCo_9S_{10}$/CNTF electrode material with recently reported flexible CNT-based composite electrodes

Materials	C_v / F cm^{-3}	Rate Capability	Cycling Stability	Ref.
RGO nanosheets/ electrospun PA66 fabrics	**38.9** F cm^{-3} at 0.5 mA cm^{-2}	**75.2%** (0.5-3 mA cm^{-2})	/	**34**
Bamboo-like O-doped porous CNTs	**254** F cm^{-3} at 0.5 mA cm^{-2}	**80.3%** (0.5-20 mA cm^{-2})	**96.9%** after 10000 cycles at **20** mA cm^{-2}	**35**
Graphite/PANI networks	**3.6** F cm^{-3} at 0.5 mA cm^{-2}	**61.9%** (0.5-5 mA cm^{-2})	/	**36**
Activated CF	**27.6** F cm^{-3} at 13 mA cm^{-2}	**66.4%** (0.5-4 mA cm^{-2})	/	**37**
CNT forest grown on unidirectional CFs	**3.4** F cm^{-3} at 11 mA cm^{-2}	/	/	**38**
CNT/RGO	**492** F cm^{-3} at 1.5 mA cm^{-2}	**52.0%** (1.5-5.2 mA cm^{-2})	**90.1%** after 10000 cycles at **5.2** mA cm^{-2}	**39**
Mesoporous VN/CNT	**12.7** F cm^{-3} at 1.1 mA cm^{-2}	**46.5%** (1.1-11 mA cm^{-2})	/	**40**
$MnCo_9S_{10}$@CNTF	**449.2** F cm^{-3} at 10 mA cm^{-2}	**82.3%** (10-80 mA cm^{-2})	**98.4%** after 10000 cycles at **80** mA cm^{-2}	**This work**

Based on the theoretical and experimental results above, the high C_v is suggested to be attributed to the following reasons:

(1) The network structure allows a small resistance and facilitates ions and electron transportation. Taking advantage of CNT network as a conductive scaffold, it facilitates fast charge transfer, the loose and porous CNT networks in the hydrogel-like film favored the diffusion of electrolyte into the internal space of the film, which can effectively enhance the utilization of electrode materials for energy storage. (2) It is demonstrated that the presence of sulfide vacancies can facilitate electrons transport, reduce the energy and contributing to the remarkably improved capacitor performance. (3) Our $MnCo_9S_{10}$ has larger sizes of the holes and S-S bond length than those for $MnCo_2S_4$, which is more favorable for enhanced electron/ion transfer kinetics. (4) The Mn^{4+}/Mn^{3+} can attract more electrons than Mn^{3+}/Mn^{2+} in an oxidation-reduction reaction.

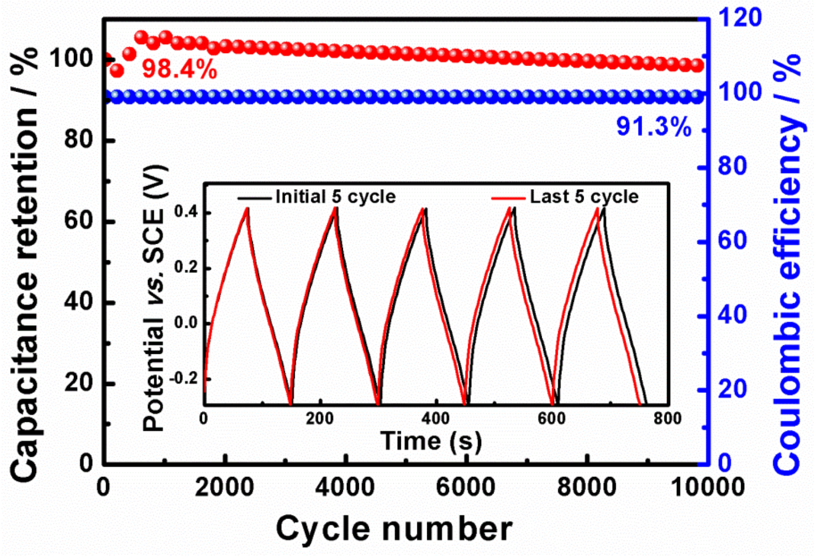

Figure 18. The cycle performance of the optimal $MnCo_9S_{10}$/CNTF electrode measured at a current density of 80 mA cm^{-2}, and the inset shows GCD curves the initial and last 5 cycles.

Long-term cycling is another critical criterion for SCs. Remarkably, 98.4% of the initial capacitance is remained after 10,000 charge/discharge cycles at a high current density of 80 mA cm^{-2} (**Figure 18**), and the charge–discharge behavior becomes stable after the 2000th cycle. The inset shows the initial and the last several periods, revealing a very regular charging–discharging behavior. Coulombic efficiency is calculated from the equation $\eta = t_d / t_c \times 100\%$, where t_c and t_d are the charge and discharge times. The coulombic efficiency is about 91.3% after 10,000 cycles. This indicates remarkable cycling stability of the electrode. After the cycling, the $MnCo_9S_{10}$ coating was still well distributed on the CNT networks, confirming the strong bonding between $MnCo_9S_{10}$ and the CNTs. On the other hand, the presence of networked channels also helped to stabilize the expansion/contraction of the film electrode during the redox reaction. In addition, the introduction of vacancies leads to faster kinetics and preserves the structure, which enables extended cycling with OH^- to occur with minimal decrease in charge storage.

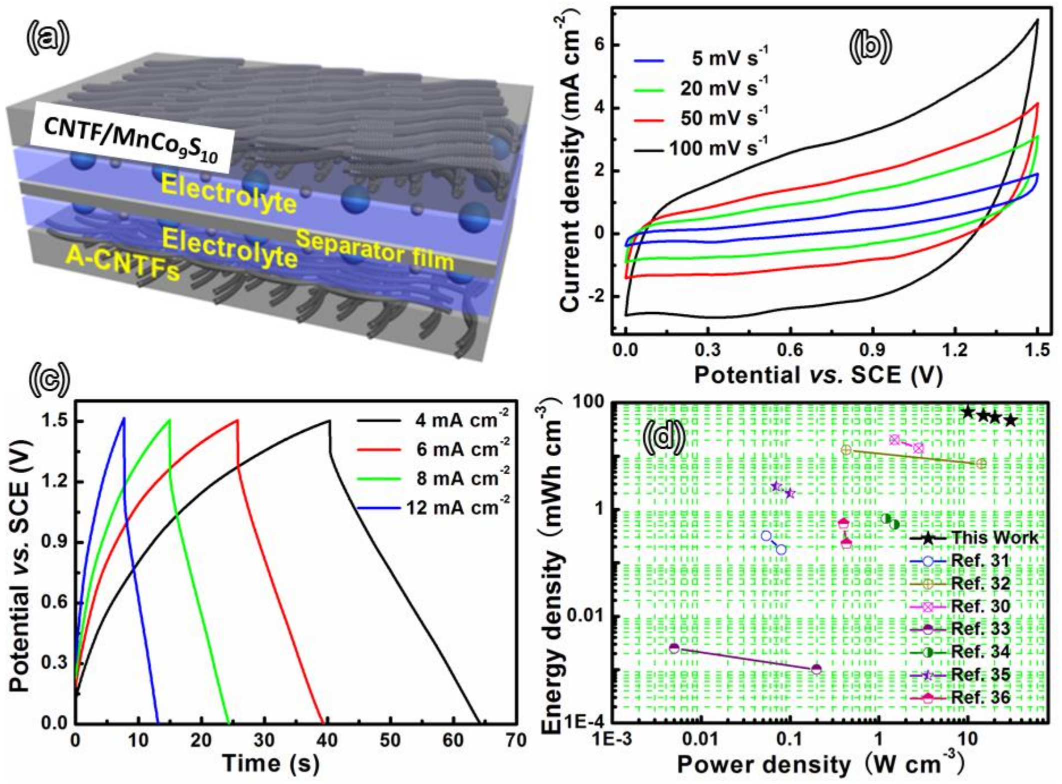

Figure 19. (a) Schematic illustration of assembled structure of an asymmetric all-solid-state CNTF/$MnCo_9S_{10}$//A-CNTFs device; (b) CV curves at various scan rates and (c) GCD curves at different current densities of the ASC device; (d) Ragone plots of the device with comparison to previous reports of asymmetric SCs with similar CNT or CF based composite electrode materials.

Figure 19a illustrates a scheme of the sandwich structure of two-electrode all-solid-state supercapacitor using the $MnCo_9S_{10}$/CNT as the positive electrode and A-CNTFs as the negative electrode. **Figure 19**b shows CV curves of the $MnCo_9S_{10}$/CNTF//A-CNTFs asymmetric SC (ASC) device at various scan rates. The CV curves’ shapes of the are smooth at all scan rates, which is different from those for the electrode. With a gradual increase of scan rate from 5 to 100 mV s^{-1}, no obvious distortion of CV curves’ shape is observed, indicating an excellent fast-charge/discharge behavior of the device. **Figure 19**c shows GCD curves of the device at various current densities, which reveals a reversible charge/discharge behavior. Specific capacitances calculated from the discharge curves are 214, 183, 170, and 149 F cm^{-3} at 4, 6, 8, and 12 mA cm^{-2}, respectively. The device achieves a high energy density of 67 mW h cm^{-3} at a power density of 10.0 W cm^{-3} (**Figure 19**d). This value is much superior over that of many solid-state SCs with similar positive electrodes. The comparison data are listed in **Table 5**. For example, this value is more than five times of that for the symmetric SC with the bamboo-like O-doped porous carbon tubes (12.9 mWh cm^{-3} at 428 mW cm^{-3})[35], ten times of that for mesoporous VN/CNT (0.54 mWh cm^{-3})[40]. Even at a power density of 30.2 W cm^{-3}, the $MnCo_9S_{10}$/CNTF//A-CNTFs ASC still delivers an energy density of 46.6 mWh cm^{-3}.

Table 1. Comparison between energy and power densities of our device and literature.

Positive electrodes	Negative electrodes	Power densities	Energy densities	Ref.
RGO/ PA66 fabrics	PA66 fabric	2.8 W cm^{-3}	14.1 mWh cm^{-3}	34
Bamboo-like O-doped porous carbon tubes	Bamboo-like O-doped porous carbon tubes	428 mW cm^{-3}	12.9 mWh cm^{-3}	35
Graphite/PANI networks	Graphite/PANI networks	54 mW cm^{-3}	0.32 mWh cm^{-3}	36
Activated CF	Activated CF	5 mW cm^{-3}	2.5 mWh cm^{-3}	37
CNT forest grown on unidirectional CFs	CNT forest grown on unidirectional CFs	1.5 W cm^{-3}	0.67 mWh cm^{-3}	38
MWCNT/RGO	MWCNT/RGO	74.3 mW cm^{-3}	2.7 mWh cm^{-3}	39
Mesoporous VN/CNT	Mesoporous VN/CNT	0.4 W cm^{-3}	0.54 mWh cm^{-3}	40
$MnCo_9S_{10}$@CNT film	A-CNTF	10.0 W cm^{-3}	67 mWh cm^{-3}	This work

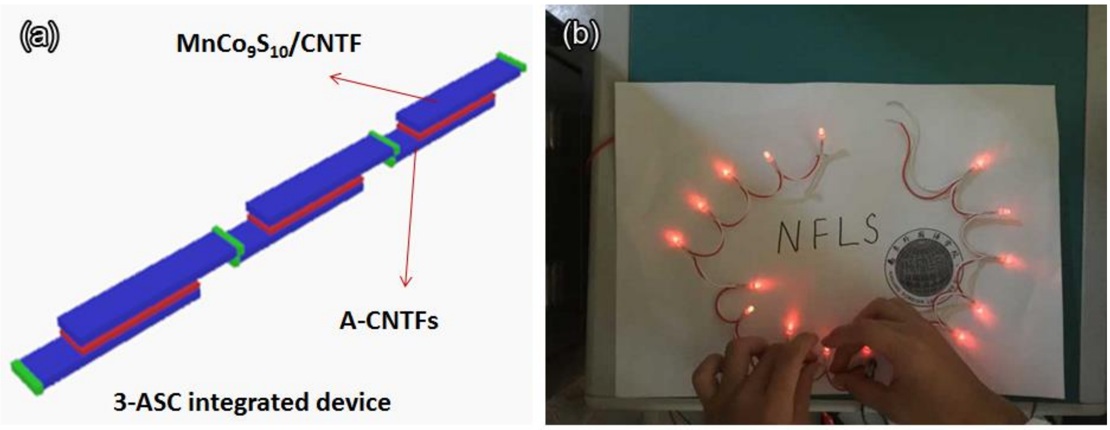

Figure 20. (a) A scheme, and (b) Digital photos showing 15 connecting LED (2 V, 20 mA) in series powered by an ASC integrated device made by combining three SCs.

The applicability can be proved visibly by powering light-emitting diodes (LEDs), as shown by digital images in **Figure 20**. We connected such advanced ASC in series to reach a high output voltage, as illustrated in **Figure 20**a. An integrated source with three connecting AECs in series can obtain a high voltage of 4.8 V allowing that they powered 15 connecting LED (2 V, 20 mA) in series, as shown in the digital photos of **Figure 20**b.

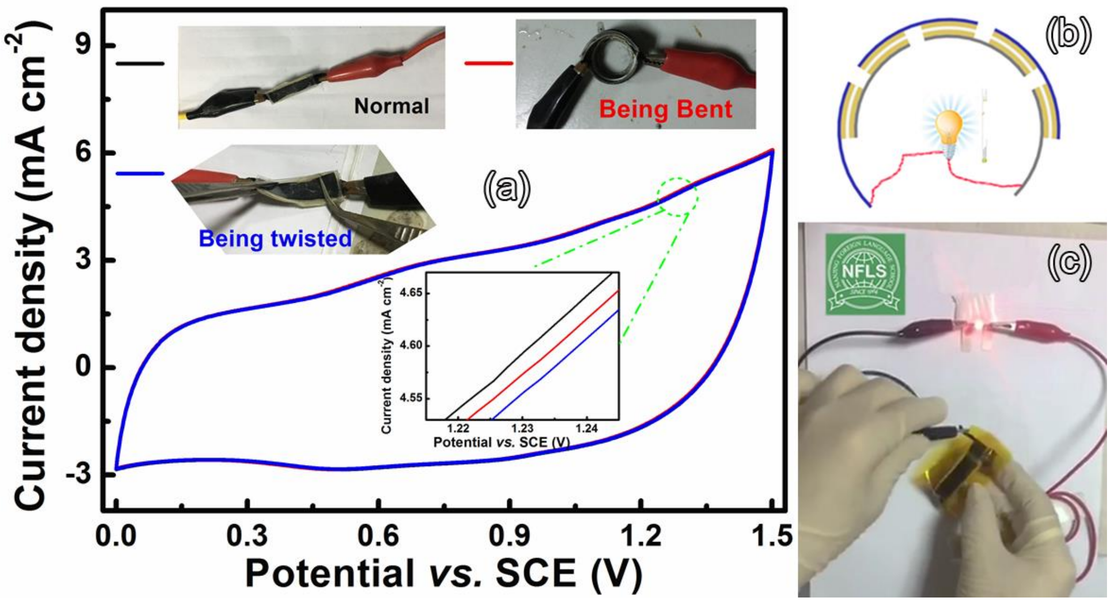

Figure 21. CV curves at a scan rate of 100 mV s^{-1} for the asymmetric device under normal, twisted and bent states. (b) The flexibility test of five CNTF/$MnCo_9S_{10}$//A-CNTFs devices connected in series. The devices are still working without structural failure and performance loss during repeated folding.

In order to further test the stability of CNTF/$MnCo_9S_{10}$//A-CNTFs devices, electrochemical behaviors of the ASC under large deformations were also evaluated. **Figure 21**a shows CV curves of the asymmetric devices under normal, twisted and bent states. There is no an obvious change in the CV curves’ shape under being bent and twisted (see the insets). In particular, in the case of folding, the device can keep the current output smoothly (**Figure 21**b). The videos showing that packaged devices are successfully operated under repeated large folding and twisting (see an attached video file). The excellent mechanical stability promises many opportunities for wearable electronics.

4. Conclusions

We demonstrated the theoretical design and synthesis of high-performing flexible electrodes based on Mn$_x$Co$_y$S$_z$/CNTFs composite films via first activation of CNTF, Mn-Co precursor growth and controlled sulfidation. The activation time was optimized to be 6 h to assure high loadings of active material, and the optimization of sulfidation leads to loosely packed nanoparticle-built porous coating. The optimal MnCo$_9$S$_{10}$/CNTF electrode has a ultrahigh volumetric capacitance reaching 450 F cm^{-3} at 10 mA cm^{-2}, much superior over previously reported values for CNT or CF based composites. Also, only 1.6% capacitance loss was observed after 10,000 cycles at a high current density of 80 mA cm^{-2}. All-solid-state CNTF/MnCo$_9$S$_{10}$//A-CNTFs ASC delivers exceptionally high energy density of 67 mW h cm^{-3} (at 10 W cm^{-3}) with an excellent cycling stability. In particular, the lightweight devices are deformable due to outstanding flexibility and stability without structural failure and performance loss even after repeated hammering and folding during discharging. This work opens a new route to high-performance CNTF-based power sources for wearable electronics.

References

[1] L. Li, Z. Wu, S. Yuan, X. B. Zhang, *Energy Environ. Sci.* **2014**, *7*, 2101.

[2] X. Xiao, X. Peng, H. Y. Jin, T. Q. Li, C. C. Zhang, B. Gao, B. Hu, K. F. Huo, J. Zhou, *Adv. Mater.* **2013**, *25*, 5091.

[3] X. L. Wang, G. Q. Shi, *Energy Environ. Sci.* **2015**, *8*, 790.

[4] X. W. Yang, C. Cheng, Y. F. Wang, L Qiu, D. Li, *Sci*. **2013**, *341*, 534.

[5] L. Kou, T. Q. Huang, B. N. Zheng, Y. Han, X. L. Zhao, K. Gopalsamy, H. Y. Sun, C. Gao, *Nat. Commun*. **2014**, *5*, 3754.

[6] Y. P. Fu, H. W. Wu, S. Y. Ye, X. Cai, X. Yu, S. C. Hou, H. Kafafy, D. C. Zou, *Energy Environ. Sci*. **2013**, *6*, 805.

[7] H. P. Cong, X. C. Ren, P. Wang, S. H. Yu, *Energy Environ. Sci*. **2013**, *6*, 1185.

[8] C. S. Du, N. Pan, *Nanotech*. **2006**, *17*, 21.

[9] H. Y. Chen, S. Zeng, M. H. Chen, Y. Y. Zhang, Q. W. Li, *Carbon* **2015**, *92*, 271.

[10] H. Y. Chen, S. Zeng, M. H. Chen, Y. Y. Zhang, L. X. Zheng, Q. W. Li, *Small* **2016**, *12*, 2035.

[11] J. T. Di, D. M. Hu, H. Y. Chen, Z. Z. Yong, M. H. Chen, Z. H. Feng, Y. T. Zhu, Q. W. Li, *ACS Nano* **2012**, *6*, 5457.

[12] H. S. Fan, H. Wang, N. Zhao, X. L. Zhang, J. Xu, *J Mater. Chem*. **2012**, *22*, 2774.

[13] P. X. Li, E. Z. Shi, Y. B. Yang, Y. Y. Shang, Q. Y. Peng, S. T. Wu, J. Q. Wei, K. l. Wang, H. W. Zhu, Q. Yuan, A. Y. Cao, D. H. Wu, *Nano Res*. **2014**, *7*, 209.

[14]S. R. Sivakkumar, J. M. Ko, Kim, D. Young, *Electrochimica. Acta* **2007**, *52*, 7377.

[15]H. Y. Chen, F. Cai, Y. Kang, S. Zeng, M. H. Chen, Q. W. Li, *ACS Appl. Mater. Interfaces* **2014**, *6*, 19630.

[16]J. Yang, C. Yu, X. M. Fan, S. X. Liang, S. F. Li, H. W. Huang, Z. Ling, C. Hao, J. S. Qiu, *Energy Environ. Sci*. **2016**, *9*, 1299.

[17]D. L. Li, Y. N. Gong, C. X. Pan, *Sci. Rep.* **2016**, *6*, 29788.

[18]M. M. Liang, M. S. Zhao, H. Y. Wang, J. F. Shen, X. P. Song, *J. Mater. Chem. A* **2018**, *6*, 2482.

[19]B. Y. Guan, L. Yu, X. Wang, S. Y. Song, X. W. Lou, *Adv. Mater.* **2017**, *29*, 1605051.

[20]S. C. Tang, B. G. Zhu, X. L. Shi, J. Wu, X. K. Meng, *Adv. Energy Mater.* **2017**, *7*, 1601985.

[21]S. E. Moosavifard, S. Fanib, M. Rahmanian, *Chem. Commun.* **2016**, *52*, 4517.

[22]T. L.Wang, M. T. Liu, H. W. Ma, *Nanomater.* **2017**, *7*, 140.

[23]J. Balamurugan, C. Li, S. G. Peera, N. H. Kima, J. H. Lee, *Nanoscale*, **2017**, *9*, 13747.

[24]J. Yang, Y. Zhang, C. C. Sun, G. L. Guo, Q. Y. Yan, X. C. Dong, *J. Mater. Chem. A* **2015**, *3*, 11462.

[25]J. A. Syed, J. Ma, B. G. Zhu, S. C. Tang, X. K. Meng, *Adv. Energy Mater.* **2017**, *7*, 1701228.

[26]K. Tao, X. Han, Q. H. Cheng, Y. J. Yang, Z. Yang, Q. X. Ma, L. Han, *Chem. Eur. J.* **2018**, *24*, 12584.

[27]Z. W. Fang, L. L. Peng, H. F. Lv, Y. Zhu, C. S. Yan, S. Q. Wang, P. Kalyani, X. J. Wu, G. H. Yu, *ACS Nano* **2017**, *11*, 9550.

[28] J. P. Perdew, K. Burke, M. Ernzerhof, *Phys. Rev. Lett.* **1996**, *77*, 3865.

[29] Z. W. Fang, L. L. Peng, Y. M. Qian, X. Zhang, Y. J. Xie, J. J. Cha, G. H. Yu, *J. Am. Chem. Soc*. **2018**, *140*, 5241.

[30] H. S. Kim, J. B. Cook, H. Lin, J. S. Ko, S. H. Tolbert, V. Ozolins, B. Dunn, *Nat. Mater.* **2016**, *16*, 454.

[31]L. N. Wang, H. Y. Chen, F. Cai, M. H. Chen, *Mater. Lett.* **2014**, *115*, 168.

[32]C. Z. Wie, Y. T. Sun, N. N. Zhan, M. Y. Liu, L. Y. Zhao, C. Cheng, D. J. Zhang, *ChemistrySelect* **2017**, *2*, 11154.

[33]J. W. Zhao, J. L. Chen, S. M. Xu, M. F. Shao, D. P. Yan, M. Wei, D. G. Evans, X. Duan, *J. Mater. Chem. A* **2013**, *1*, 8836.

[34]Y. S. Wang, S. M. Li, S. T. Hsiao, W. H. Liao, P. H. Chen, S. Y. Yang, H. W. Tien, C. C. M. Ma, C. C. Hu, *Carbon* **2014**, *73*, 87.

[35]Z. Y. Xu, Y. J. Liu, H. B. Chen, M. Yang, H. M. Li, *J Mater. Sci.* **2017**, *52*, 7781.

[36] B. Yao, L. Y. Yuan, X. Xiao, J. Zhang, Y. Y. Qi, J. Zhou, J. Zhou, B. Hu, W. Chen, *Nano Energy* **2013**, *2*, 1071.

[37] W. J. Ma, S. H. Chen, S. Y. Yang, W. P. Chen, W. Weng, M. F. Zhu, *ACS Appl. Mater. Interfaces* **2016**, *8*, 14622.

[38] J. Cherusseria, K. K. Kar, *RSC Adv.* **2015**, *5*, 34335.

[39]G. Z. Sun, X. Zhang, R. Z. Lin, B. Chen, L. X. Zheng, X. Huang, L. Huang, W. Huang, H. Zhang, P. Chen, *Adv. Electron. Mater.* **2016**, *2*, 1600102.

[40]X. Xiao, X. Peng, H. Y. Jin, T. Q. Li, C. C. Zhang, B. Gao, B. Hu , K. F. Huo, J. Zhou, *Adv. Mater.* **2013**, *25*, 5091.

Acknowledgments

The authors would like to appreciate the guidance and instructions of my instructor Dr. Liangliang Xu who directed the study. We thank Prof. Shaochun Tang and his research group of *Electrochemical Energy Materials & Devices*, especially Mr. Weijie Song and Dr. Gang Chen for their help on the experiments, valuable discussions, and paper writing, and facilities/instruments at National Laboratory of Solid State Microstructures, College of Engineering and Applied Sciences, Nanjing University. Prof. Shaochun Tang provided the research lab and resources, and offered valuable feedbacks for my academic writing; Mr. Weijie Song gave me instructions during the experiments, and he also conducted the research of synthesizing the pristine CNTFs, which is the basics of this research. We also thank Prof. Hao Dong and his research group of *Theoretical Chemistry*, Kuang Yaming Honors School, Nanjing University, especially Dr. Dongbo Zhao for their help on the theoretical calculations.

Group Members' Contributions

Yuewei Zhou carried out main parts of the experiments including synthesis of Mn-Co Precursor@CNTFs and $Mn_xCo_yS_z$@CNTF as well as electrochemical performance measurements; Hanyue Wang contributed in preparing of flexible all-solid-state SCs, materials characterizations, and carrying out electrochemical performance measurements; Shiwen Fang contributed in the theoretical calculations based on the DFT method and participated in some experiments. Yuewei Zhou wrote the paper, and all authors collectively participated in discussing and reviewing of the paper. Dr. Liangliang Xu and Prof. Shaochun Tang revised the paper.

南京外国语学校
“超容”小分队队员简介

（左起：周阅微、方世文、王涵悦）

团队介绍：

周阅微、王涵悦、方世文同学来自南京外国语学校高中部，成绩优异，全面发展，是学校 STEM 课程核心成员，在化学、物理、数学等学科取得诸多奖项及荣誉。出于共同学术兴趣，3 人于 2017 年组建小组，围绕柔性超级电容器存在的科学问题，开展了电极理论设计、制备及固态器件研究。3 人同时入选中国科协、教育部 2018 年度中学生“英才计划”，参加国际学术研讨会，撰写科研论文，极大提升了科学素养，开阔了学术视野。

队员一：周阅微，南京外国语学校高二

姓名：周阅微

性别：男

就读学校：

2008.09—2014.06 南京市琅琊路小学

2014.09—2017.06 南京外国语学校初中部

2017.09 至今 南京外国语学校高中部

学术经历及荣誉奖项：

1. 南京外国语学校 STEM 课程成员（实验化学），2017.09 至今
2. 中国科协、教育部 2018 年度中学生“英才计划”人选（化学学科），2017.12
3. 英国皇家化学学会化学新星挑战赛(RSC3)华东区金奖，2017.12
4. 被南京外国语学校推荐为 2019 年度中学生“英才计划”（化学学科）人选，2018.11
5. 2018 年度中学生“英才计划”全国化学论坛推荐人选(全省 2 人)，中国科技大学，2018.11
6. iGEM 铜奖，2018.10
7. 申请发明创造专利一项——“一种简易去除空气中雾霾及可溶性异味物质的装置”（专利号：201721303763.9）
8. 南京市青少年科技奖三等奖，2017.11

队员二：王涵悦，南京外国语学校高二

姓名：王涵悦

性别：女

就读学校：

2008.09—2014.06　南京市琅琊路小学

2014.09—2017.06　南京市外国语学校初中部

2017.09 至今　南京市外国语学校高中部

学术经历及荣誉获奖：

1. 南京外国语学校“周恩来”奖学金特长发展奖，2016
2. 南京外国语学校“周恩来”奖学金全面发展奖，2017
3. 获“时代杯”初中数学文化节一等奖，2016
4. 获“随园杯”初中物理竞赛一等奖，2017
5. 获南京市优秀学生干部称号，2016-2017
6. 南京外国语学校 STEM 课程成员（物理），2017-2018
7. 中国科协、教育部 2018 年度中学生“英才计划”（物理学科）2017.12
8. 第二届全国中学生物理学术创新邀请赛（NYPT-2）、第六届江苏省中学生物理学术创新竞赛（JSYPT-6）团体特等奖，2018
9. iGEM 铜奖，2018.10
10. 全国语言学奥林匹克竞赛二等奖,2018.10
11. 开展多能源互补微电网系统的协调控制研究（2017）、微电网多元储能系统设计及石墨烯电池的应用研究（2018）、全国中学生“英才计划”南京大学物理项目——准同型相界调控压电材料研究（2018）
12. 全国“英才计划”冬令营集训，厦门大学，2018

队员三：方世文（Owen）,南京外国语学校高二

姓名：方世文（Owen）

性别：男

就读学校：

2008.09—2014.06　南京外国语学校仙林分校小学部

2014.09—2017.06　南京外国语学校初中部

2017.09 至今　南京外国语学校高中部

学术经历及荣誉奖项：

1. 获“时代杯”初中数学文化节一等奖，2016
2. 获全国初中数学联赛一等奖，2016
3. 南京外国语学校“周恩来”奖学金特长发展奖，2016
4. 获 2017 年度全国初中应用物理竞赛一等奖，2017
5. 中国科协、教育部 2018 年度中学生“英才计划”（物理学科）2017.12
6. 美国杯物理竞赛获优秀奖，2018
7. Nanjing International Physics Challenge 2018“Silver Award”，2018
8. 第二届全国中学生物理学术创新邀请赛（NYPT-2）、第六届江苏省中学生物理学术创新竞赛（JSYPT-6）荣获团体特等奖，2018
9. 全国中学生“英才计划”南京大学物理项目——准同型相界调控压电材料研究，2018